Petroleum Science 22 (2025) 4555–4572

Contents lists available at ScienceDirect

Petroleum Science

journal homepage: www.keaipublishing.com/en/journals/petroleum-science

Original Paper

Quantitative evaluation of brittleness anisotropy and its influencing factors in terrestrial shale

Jian-Yong Xie [a,b,*], Yan-Ping Fang [a,b], Chun-Wei Wu [a,b], She-Bao Jiao [c], Jing-Xiao Wang [a,b], Ji-Xin Deng [a,b], Xing-Jian Wang [a,b]

[a] State Key Laboratory of Oil and Gas Reservoir Geology and Exploitation, Chengdu University of Technology, Chengdu, 610059, Sichuan, China
[b] Key Lab of Earth Exploration & Information Techniques of Ministry of Education, Geophysical Institute, Chengdu University of Technology, Chengdu, 610059, Sichuan, China
[c] CNOOC China Limited Shanghai Branch, 200050, Shanghai, China

ARTICLE INFO

Article history:
Received 21 April 2025
Received in revised form
17 June 2025
Accepted 30 July 2025
Available online 9 August 2025

Edited by Meng-Jiao Zhou

Keywords:
Shale reservoir
Organic matter
Brittleness anisotropy
Theoretical and experimental rock physics

ABSTRACT

Brittleness is pivotal in predicting shale reservoir quality and designing hydraulic fracturing strategies. However, intricate diagenetic environment of shale, characterized by distinct bedding structures, challenges the isotropic-based brittleness assessment methods. This study introduces a new quantitative approach to assess shale brittleness anisotropy, integrating anisotropic elastic responses and tensile fracturing mechanisms. The proposed model effectively reduces uncertainty in the causal relationship between Young's modulus and brittle failure. Comprehensive experimental validation encompassed 18 samples from six groups of Chang 7 terrestrial shale in Ordos Basin. The optimal anisotropic tensile strength criterion (N-Z criterion, error < 5%) was identified, enhancing the theoretical accuracy of the proposed model. Comparative experimental results demonstrate that the model adeptly predicts brittleness strength and directional variation characteristics across variations in mineral type, content and microstructure, underscoring its effectiveness. Additionally, theoretical predictions on shale samples with different organic matter reveal that brittleness strength and its anisotropy across varying OM are not monotonously decreasing. The research highlights that brittleness characteristics are influenced by both mineral type/content and microstructural distribution. Notably, the prevalence of isotropic brittle minerals is the primary determinant of brittleness strength, positively correlated. Conversely, ductile mineral content (striped skeletal support-type OM and clay) negatively correlates with brittleness strength, acting as secondary controlling factors. The impact of pore-filled OM on brittleness appears negligible. Rock physical modeling based on equivalent media theory for shale with pore-filled and/or striped OM further elucidates the mechanisms driving these variations. These findings attach great importance in assessment of terrestrial shale geological and engineering "sweet-spots".

1. Introduction

The strategic significance of unconventional shale oil and gas reservoirs has progressively influenced the global energy landscape. Effective exploration and development play a crucial role in promoting the sustainable development of the energy industry, enhancing energy supply security, and achieving "dual carbon" environmental goals (Cooper et al., 2016; Feng et al., 2019, 2020; Mandal et al., 2022; Wan et al., 2022). Accurate prediction of high-quality reservoirs and fracture design in the exploration and development of shale oil and gas resources relies on the effective assessment of geological and engineering "sweet spots" (Gale et al., 2007; Guo, 2016). Brittle parameters, as one of the most critical characterization factors in the identification and prediction of dual "sweet spots" serve as important indicators for selecting high-quality shale oil and gas reservoirs and assessing their development potential (Ai et al., 2016; Kivi et al., 2018). Shale oil

* Corresponding author.
E-mail address: xjyshl@sina.com (J.-Y. Xie).
Peer review under the responsibility of China University of Petroleum (Beijing).

https://doi.org/10.1016/j.petsci.2025.07.026

Nomenclature

$\mathbf{C}_{ij}^{\theta}$	Elastic coefficients at an inclination angle
ε_{zz}	Axial positive strain
σ_{zz}	Axial stress
$T(\theta)$	Tensile strength anisotropy
SEM	Scanning electron microscopy
DEM	Differential effective-medium
γ	S-wave anisotropic parameter
$\mathbf{M}_{\theta}$	Transformation matrix
$E(\theta)$	Young's modulus in direction θ
T_{90}	Tensile strength parallel to bedding
$\mathbf{C}_{ij}^{0}$	Inverse of the compliance matrix
$\nu_{\max}(\theta)$	Maximum Poisson's ratio anisotropy
$\nu_{\min}(\theta)$	Minimum Poisson's ratio anisotropy
$B_{\mathrm{E}}(\theta)$	Brittleness anisotropy at elastic stage
SCA	Self-consistent approximation
ε	P-wave anisotropic parameter
ΔB	Brittleness anisotropic parameter
TOC	Total organic carbon
T_0	Tensile strength 90° to bedding
θ^*	Critical angle of weak plane

and gas reservoirs exhibit strong heterogeneity and physical properties such as low porosity and permeability (Yan et al., 2023). Brittle characteristics play a critical role in determining the mechanical behavior of reservoir rocks and directly impact wellbore stability. Moreover, during reservoir stimulation-particularly hydraulic fracturing aimed at enhancing production—brittleness serves as a key parameter for evaluating rock fracturability and guiding the development of effective fracture networks. As such, comprehensive research into brittleness characteristics and their evaluation methods is of both scientific and practical importance for the exploration, development, and sustained production of shale oil and gas reservoirs (Jarvie et al., 2007; Yuan et al., 2013; Zhang et al., 2016).

The current definition of rock brittleness lacks a comprehensive definition considering both mechanical characteristics and controlling mechanisms of influencing factors. Studies indicate that mechanically, brittle rocks typically exhibit characteristics such as low load extension rates and high internal friction angles (Hucka et al., 1974), distinct fracture surfaces during failure (Hajiabdolmajid et al., 2003), the generation of finer particles and cracks under loading (Nygård et al., 2006), high rebound energy, and a high compressive-to-tensile strength ratio (Jarvie et al., 2007). Additionally, they display high Young's modulus and low Poisson's ratio (Rickman et al., 2008; Goodway et al., 2010). In this basis, various mechanical characterization methods for brittleness in isotropic backgrounds are proposed. Altindag (2002) established a brittleness index based on fracture toughness through equation significance testing. Rickman et al. (2008) proposed a brittleness evaluation method calculated by normalizing the Poisson's ratio and Young's modulus in specific regions. Yagiz (2009) developed a function relating brittleness index to tensile and compressive strength using penetration tests combined with fuzzy reasoning and nonlinear regression. Parney and Lange (2010) characterized the brittleness zone of Wattenberg shale using Young's modulus (E) and Poisson's ratio (v) calculated from longitudinal and shear wave impedances. Guo et al. (2015) considered the impact of rock mechanical properties on brittleness and proposed a comprehensive brittleness index integrating Young's modulus, Poisson's ratio, and fracture toughness. Liu et al. (2019) established a new brittleness index model based on the energy conversion relationship in stress-strain curves, including pre-peak and post-peak brittleness indices and an overall brittleness index. Chen et al. (2020) considered the elastic energy accumulation and release throughout the entire rock loading-to-failure process and developed a brittleness index based on the overall energy evolution process. Kuang et al. (2021) combined the definition of brittleness with rock material failure mechanisms, considering stress growth and decay rate characteristics, and established a brittleness index based on total stress-strain. Xie et al. (2023) proposed a new quantitative brittleness model for shale based on significance assignment of the brittle-sensitive index (BSI) at different stage during the loading by energy evolution-based fuzzy analytic hierarchy process. Brittleness evaluation methods grounded in rock mechanical behavior have proven effective in characterizing energy absorption, dissipation, and the micromechanical processes governing deformation and failure before and after rock fracture. However, these approaches face significant limitations in accurately capturing the influence of complex factors such as in-situ environmental conditions, stress regimes, and tectonic deformation, all of which can profoundly affect shale behavior.

Researches indicate that the layering structure formed during the diagenetic process, influenced by the spatial orientation distribution of clay minerals, kerogen, and fractures, results in apparent anisotropic features in the full-scale elastic wave responses observed during shale oil and gas reservoir exploration processes (Vernik et al., 1992; Wang, 2002; Tsvankin et al., 2010; Xie et al., 2015, Baird et al., 2017; Wu et al., 2020). Concurrently, the elastic mechanical properties, strength characteristics, and fracture patterns in shale reservoir development also exhibit significant anisotropy due to the influence of weak planes within the strata (Niandou et al., 1997; Nasseri et al., 2003; Colak et al., 2004; Li et al., 2020; Zhao et al., 2024). Consequently, neglecting the impact of anisotropic characteristics in the exploration and development of shale reservoirs may lead to poor imaging effects, inaccurate predictions of high-quality reservoirs, and serious stability issues such as wellbore collapse and leakage. In response to this challenge, numerous scholars have proposed that the brittleness characteristics of shale may also exhibit directional variations. They have conducted a series of exploratory studies through experimental testing and theoretical derivations. Hou et al. (2016) evaluated the anisotropic brittleness characteristics of Longmaxi shale using stress-strain curves obtained from triaxial rock mechanics experiments. Geng et al. (2016) studied the variability of brittleness with azimuthal angle changes based on rock mechanics tests on shale samples cored at different angles and explored the trends under different confining pressures. Combined with uniaxial strength test data, Wang et al. (2017) investigated the directional variations of brittleness in Longmaxi shale based on the brittleness index calculated using the strength parameter method. Yang et al. (2020) analyzed the brittleness characteristics of shale specimens under different bedding dip angles and confining pressures based on stress-strain curves and energy evolution laws during loading. Jamshidi et al. (2021) performed experimental measurement on rock samples at different angles using Brazilian mechanics and uniaxial compression tests, obtaining discrete trends in brittleness anisotropy. Gui et al. (2023) studied the brittleness variation characteristics of Longmaxi shale based on uniaxial compression

tests and well logging data, investigating the influence of total organic carbon (TOC) content on anisotropic brittleness values. On the theoretical research front, Luan and Xie (2014) introduced a transition matrix to achieve corresponding transformations and derived anisotropic expressions for Young's modulus and Poisson's ratio with respect to azimuthal angles. Zhang et al. (2016) further incorporated the influence of azimuthal angles to derive anisotropic expressions for Young's modulus and Poisson's ratio with respect to dip and azimuthal angles. Gui et al. (2023) assumed shale as a transversely isotropic medium and derived theoretical expressions for the anisotropic variations of Young's modulus and Poisson's ratio along the uniaxial loading direction based on elastic constitutive equations. Normalization methods were employed to obtain theoretical formulas characterizing the directional variations of brittleness.

In summary, most existing brittleness assessment methods are developed based on the mechanical behavior of brittle rocks under isotropic conditions, which limits their applicability in characterizing the anisotropy inherent to shale formations. This anisotropy arises from complex diagenetic processes, heterogeneous reservoir conditions, and varied burial histories. While some studies have attempted to account for directional variations in shale brittleness—primarily through core experiments conducted at multiple orientations or by applying anisotropic formulations based on Young's modulus and Poisson's ratio—each approach has limitations. Core-based methods, although offering direct insights into directional brittleness, often produce scattered datasets with limited consistency and lack a unified theoretical framework for predictive modeling. Moreover, they require strict experimental controls and are challenging to scale in practical reservoir evaluation. The latter primarily constructs theoretical frameworks in the context of brittle rocks exhibiting high Young's modulus and low Poisson's ratio, reflecting directional changes in pre-damage elastic responses (E, ν). However, these formulations fail to capture post-damage brittle fracture patterns and do not quantitatively consider the influence of elastic deformation and fracture mechanisms on shale brittleness anisotropy. In fact, previous research suggests that a high Young's modulus may render rocks more resistant to brittle fracture (Kartashov, 1978; Cho and Perez, 2014; Salah et al., 2019). Consequently, relying solely on brittleness anisotropy theories established during the elastic loading stage may be challenging to ensure applicability. Despite the awareness of this issue by Wang et al. (2015) and Salah et al. (2019), who attempted to address the causality contradiction by introducing a critical tensile stress equation on the basis of Luan and Xie (2014) proposed brittleness anisotropy equation, the tensile stress formula is directly derived from isotropic expressions, lacking rigorous theoretical derivation and requiring further scrutiny regarding its applicability. The effectiveness and accuracy of the corresponding brittleness anisotropy equations have not undergone systematic experimental validation. Moreover, the relationship between kerogen components in shale reservoir rocks and brittle characteristics is complex. Different structures and content levels are bound to influence the directional variations in brittleness patterns, yet reports on their correlation and response mechanisms are scarce (Wang et al., 2015).

This study comprehensively considers the anisotropic elastic response mechanism and fracture mechanisms throughout the loading process to establish a novel theoretical model for anisotropic brittleness in terrestrial shale. Firstly, based on the transversely isotropic constitutive equations during the elastic phase, combined with Bond transformation derivations, theoretical equations are derived for three strains in the spatially vertical direction as functions of the angle. Subsequently, anisotropic equations for Young's modulus and formulas for maximum and minimum Poisson's ratios along the loading direction are further derived. By normalization, an anisotropic equation for brittleness during the elastic phase is established. Simultaneously, considering the geological characteristics of terrestrial shale in the study area, experimental test data are compared with numerous existing anisotropic formulas for tensile strength in terrestrial shale. The most applicable and accurate formula is selected and incorporated into the novel anisotropic brittleness model. Ultimately, theoretical equations representing the directional variations in brittleness elastic and fracture responses throughout the loading process are constructed.

On this basis, the effectiveness and accuracy of the proposed anisotropic brittleness model are validated using physical and mechanical tests conducted on terrestrial shale cores from the seventh member of the Yanchang Formation (Late Triassic) in the Ordos Basin, China. addition, quantitative rock physics experiments are performed to investigate the influence of kerogen on directional variations in shale brittleness. These experimental results are further integrated with anisotropic rock physics modeling based on effective medium theory, enabling a deeper analysis of the underlying response mechanisms governing the observed anisotropic behavior.

2. Anisotropic brittleness model for shale

Brittleness parameters serve as not only crucial characterization factors for identifying and predicting the geological sweet-spots but also as important indicators for selecting high-quality engineering sweet-spots in shale oil and gas reservoir. Therefore, an effective brittleness evaluation method needs to simultaneously consider the brittleness characteristics during both the elastic stage and the fracture process. Similarly, the establishment of an effective theoretical model for anisotropic brittleness must comprehensively consider the elastic anisotropic response mechanism and anisotropic brittle fracture mechanisms. In the elastic stage, the brittleness of shale is predominantly influenced by the inherent characteristics of the rock, including mineral composition, particle-particle contact relationships, and pore features that manifest mechanical responses under stress. During this stage, Young's modulus and Poisson's ratio can characterize the mechanical responses resulting from different combinations of mineral components, thereby describing the brittleness variations caused by factors such as the framework and pores. In this context, shale is considered as a transversely isotropic (VTI) medium (Fig. 1(a)). When the rock specimen is subjected to a uniaxial stress from the Z-direction, according to Hooke's law, the stress-strain relationship can be expressed as follows (Wittke, 1990):

$$\sigma = \mathbf{C}_{ij}^{\theta} \cdot \varepsilon \tag{1}$$

The elastic coefficients $\mathbf{C}_{ij}^{\theta}$ for shale at an inclination angle θ can be determined using the elastic coefficients of the VTI medium, denoted as $\mathbf{C}_{ij}^{0}$, through Bond transformations. The specific relationship is given by

$$\mathbf{M}_{ij}^{\theta} = \mathbf{M}_{\theta} \mathbf{C}_{ij}^{0} \mathbf{M}_{\theta}^{\mathrm{T}} \tag{2}$$

where $\mathbf{M}_{\theta}$ is the transformation matrix used for the Bond transformation (Mavko et al., 2009). This matrix allows the conversion of the VTI medium to any TTI medium with its symmetry axis inclined at an angle θ. Here, $\mathbf{C}_{ij}^{0}$ represents the inverse of the compliance matrix $\mathbf{S}_{ij}^{0}$ or the VTI medium, and the expression for $\mathbf{S}_{ij}^{0}$

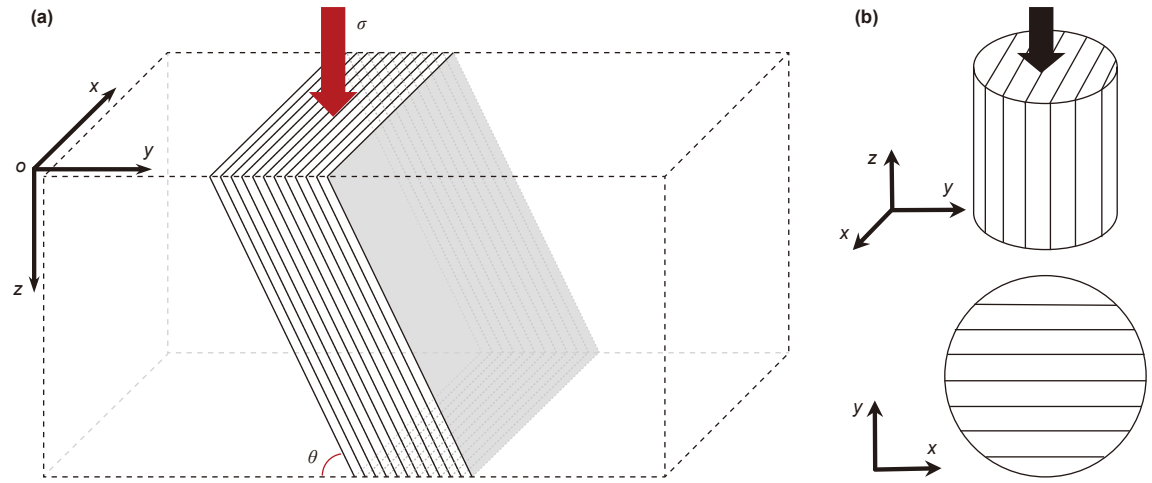

Fig. 1. **(a)** Sketch of shale layers at different angles. (x, y, z) is the basic cartesian coordinate system. The shale layers (shaded part) are assumed to be transversely isotropic media, and the angle between shale layers and plane XOY is θ. **(b)** Sketches of compression and expansion in different directions.

is as follows (Ong et al., 2016; Alejano et al., 2021; Khaledi et al., 2023):

$$\mathbf{S}_{ij}^{0}=\left(\mathbf{C}_{ij}^{0}\right)^{-1}=\begin{bmatrix} \frac{1}{E_{11}} & \frac{-\nu_{12}}{E_{11}} & \frac{-\nu_{13}}{E_{33}} & 0 & 0 & 0 \\ \frac{-\nu_{12}}{E_{11}} & \frac{1}{E_{11}} & \frac{-\nu_{13}}{E_{33}} & 0 & 0 & 0 \\ \frac{-\nu_{13}}{E_{33}} & \frac{-\nu_{13}}{E_{33}} & \frac{1}{E_{33}} & 0 & 0 & 0 \\ 0 & 0 & 0 & \frac{1}{\mu_{13}} & 0 & 0 \\ 0 & 0 & 0 & 0 & \frac{1}{\mu_{13}} & 0 \\ 0 & 0 & 0 & 0 & 0 & \frac{2+2\nu_{12}}{\mu_{12}} \end{bmatrix} \tag{3}$$

By substituting Eqs. (2) and (3) into Eq. (1) and simplifying, we obtain:

$$\varepsilon_{xx}(\theta)=\left[\sin^2\theta\cos^2\theta\left(\frac{1}{E_{11}}+\frac{1}{E_{33}}-\frac{1}{\mu_{13}}\right)-\left(\sin^4\theta+\cos^4\theta\right)\frac{\nu_{13}}{E_{33}}\right]\sigma_{zz} \tag{4}$$

$$\varepsilon_{yy}(\theta)=\left(-\frac{\nu_{12}}{E_{11}}\sin^2\theta-\frac{\nu_{13}}{E_{33}}\cos^2\theta\right)\sigma_{zz} \tag{5}$$

$$\varepsilon_{zz}(\theta)=\left[\frac{\sin^4\theta}{E_{11}}+\frac{\cos^4\theta}{E_{33}}+\sin^2\theta\cos^2\theta\left(\frac{1}{\mu_{13}}-\frac{2\upsilon_{13}}{E_{33}}\right)\right]\sigma_{zz} \tag{6}$$

According to the definition, the Young's modulus is equal to the ratio of uniaxial stress to uniaxial strain. Therefore, the Young's modulus in the Z direction is:

$$\mathrm{E}(\theta)=\frac{\sigma_{zz}(\theta)}{\varepsilon_{zz}(\theta)}=\frac{1}{\frac{\sin^4\theta}{E_{11}}+\frac{\cos^4\theta}{E_{33}}+\sin^2\theta\cos^2\theta\left(\frac{1}{\mu_{13}}-\frac{2\upsilon_{13}}{E_{33}}\right)} \tag{7}$$

As shown in Fig. 1(b), the Poisson's ratio is the ratio of transverse positive strain to axial positive strain when the material is subjected to uniaxial tension or compression. The axial positive strain is denoted as ε_{zz}, while the transverse positive strain occurs in the XOY plane direction. Furthermore, each direction has a different strain within the XOY plane. Through calculations, it is found that the Poisson's ratio is maximum in the X direction and minimum in the Y direction, namely:

$$\begin{aligned}\nu_{\max}(\theta)=\nu_x(\theta)&=\frac{\varepsilon_{xx}(\theta)}{\varepsilon_{zz}(\theta)}\\&=\frac{\sin^2\theta\cos^2\theta\left(\frac{1}{E_{11}}+\frac{1}{E_{33}}-\frac{1}{\mu_{13}}\right)-\left(\sin^4\theta+\cos^4\theta\right)\frac{\nu_{13}}{E_{33}}}{\frac{\sin^4\theta}{E_{11}}+\frac{\cos^4\theta}{E_{33}}+\sin^2\theta\cos^2\theta\left(\frac{1}{\mu_{13}}-\frac{2\upsilon_{13}}{E_{33}}\right)}\end{aligned} \tag{8}$$

$$\nu_{\min}(\theta)=\nu_y(\theta)=\frac{\varepsilon_{yy}(\theta)}{\varepsilon_{zz}(\theta)}=\frac{-\frac{\nu_{12}}{E_{11}}\sin^2\theta-\frac{\nu_{13}}{E_{33}}\cos^2\theta}{\frac{\sin^4\theta}{E_{11}}+\frac{\cos^4\theta}{E_{33}}+\sin^2\theta\cos^2\theta\left(\frac{1}{\mu_{13}}-\frac{2\upsilon_{13}}{E_{33}}\right)} \tag{9}$$

Here, $\nu_{\max}(\theta)$ represents the ratio of strain perpendicular to the stress direction and parallel to the bedding direction to the strain in the loading direction (i.e., the equation for maximum Poisson's ratio anisotropy), and $\nu_{\min}(\theta)$ represents the ratio of strain perpendicular to the stress direction and parallel to the bedding direction to the strain in the loading direction (i.e., the equation for minimum Poisson's ratio anisotropy).

Grieser and Bray (2007) proposed that brittle rocks tend to exhibit a lower Poisson's ratio (indicating the rock's ability to fail under load) and a higher Young's modulus (measuring its ability to sustain fracture). Based on this, a brittleness anisotropic equation at elastic stage is constructed by combining the Rickman method (Rickman et al., 2008) to normalize the Poisson's ratio and Young's modulus:

$$E_{\mathrm{n}}(\theta)=\frac{E(\theta)-E_{\min}}{E_{\max}-E_{\min}} \tag{10}$$

$$\nu_{\mathrm{n}}(\theta)=\frac{\nu_{\max}-\nu(\theta)}{\nu_{\max}-\nu_{\min}} \tag{11}$$

$$B_{\mathrm{E}}(\theta)=\frac{\nu_{\mathrm{n}}(\theta)+E_{\mathrm{n}}(\theta)}{2} \tag{12}$$

where E_{max} and E_{min} represent the maximum and minimum values of Young's modulus, and ν_{max} and ν_{min} represent the maximum and minimum values of Poisson's ratio in the corresponding region. $E_n(\theta)$ and $\nu_n(\theta)$ represent the normalized Young's modulus anisotropy equation and Poisson's ratio anisotropy equation, respectively. $B_E(\theta)$ represents the theoretical equation for brittleness anisotropy at the elastic stage. It should be noted that VTI media under uniaxial stress can derive Poisson's ratio anisotropy equations in two directions, i.e., Eqs. (8) and (9). By substituting them into Eqs. (10)–(12), two brittleness anisotropy equations can be obtained. Considering that a lower Poisson's ratio reflects a lower load required for rock fracture, showing a greater brittle characteristic under the same stress, the constructed brittleness anisotropy equations under the same stress should more directly characterize the initial fracture orientation of shale. This is also more helpful for the design of hydraulic fracturing parameters in the shale oil and gas development process. Therefore, in Eq. (12), we choose ν_{min} as the Poisson's ratio anisotropy equation.

In the previous discussion, considering only the brittleness anisotropic equation during the elastic stage may fails to characterize the brittleness directional variation during the fracture stage.

Therefore, introducing the tensile strength anisotropy equation supplements the brittleness anisotropic equation from elastic mechanism. Simultaneously, the introduction of the tensile strength anisotropy equation can effectively address the well-documented paradox in rock mechanics where a high Young's modulus E, typically associated with stiff and “brittle” behavior in elastic theory, does not necessarily correspond to a higher propensity for brittle failure in real shale formations (Kartashov, 1978; Cho and Perez, 2014). While high E reflects increased resistance to elastic deformation (i.e., greater stiffness), it also implies a stronger resistance to strain localization and crack initiation-key precursors to brittle fracture. Consequently, stiff rocks may store more elastic energy but require higher stress to initiate fracture, making them potentially less fracture-prone under given stress conditions. This leads to the so-called “stiff-but-tough” behavior observed in some laminated or quartz-rich shales. To overcome this contradiction, our model decouples stiffness from fracture susceptibility by introducing a tensile strength anisotropy function $T(\theta)$ into the denominator of the brittleness index formulation. This modification enables the model to realistically reduce brittleness predictions in stiff, fracture-resistant directions while elevating them in mechanically weaker orientations-more accurately reflecting the micromechanical behavior and fracture risk observed in experimental shale samples. In this basis, the present study relies on mechanical testing data of shale rocks in the research area and employs various theoretical equations for tensile strength anisotropy to compare and analyze errors. These include the N-Z criterion (Nova and Zaninetti, 1990), SPW (single plane weakness) criterion (Jaeger, 1960), L-P criterion (Lee and Pietruszczak, 2015), and CPA (critical plane anisotropy) criterion (Lee and Pietruszczak, 2015). The research indicates that the tensile strength anisotropy criterion proposed by Nova and Zaninetti in 1990 (N-Z criterion, Nova and Zaninetti, 1990) demonstrates favorable characterization performance. Comparative analysis results will be presented in the next section, and the specific expression for the N-Z criterion ($T(\theta)$) is provided below:

$$T(\theta)=\frac{T_0T_{90}}{T_0\sin^2\theta+T_{90}\cos^2\theta} \tag{13}$$

where T_0 and T_{90} are the tensile strength in the direction perpendicular and parallel to the bedding plane, respectively. Integrating Eq. (12) and Eq. (13) yields a comprehensive expression of the brittleness anisotropic theoretical equation:

$$B(\theta)=\frac{B_E(\theta)}{T(\theta)} \tag{14}$$

where $B_E(\theta)$ represents the theoretical equation for brittleness anisotropy at the elastic stage, and $T(\theta)$ denotes anisotropic equation for tensile strength at failure stage. This formulation explicitly separates the elastic energy accumulation potential (represented by $B_E(\theta)$) from the fracture initiation threshold (controlled by $T(\theta)$), allowing the model to reflect both pre-failure deformation and post-peak fracture behavior. It ensures that brittleness increases only when both elastic stiffness and low fracture resistance align in the same direction. This dual-mechanism formulation better captures the anisotropic fracture characteristics observed in experimental data and supports a more physically meaningful interpretation of directional brittleness in shale. In the following, the effectiveness and accuracy of the selected $T(\theta)$ and the proposed brittleness anisotropic equation will be validated using experimental testing data from natural shale samples in the research area.

3. Experimental validation of the quantification model

3.1. Sample descriptions and experimental methodology

To validate the applicability and effectiveness of the proposed tensile strength anisotropic equation and novel brittleness anisotropic model for lacustrine shale. Experimental measurements of elastic properties and strength properties are conducted on 6 sets of natural shale samples (labeled as #B1, #B2, #B3 and #K1, #K2, #K3). Each set comprised three plugs, each with a diameter of 25 mm and a height of 50 mm, obtained from different orientations (0°, 45°, 90°) relative to the bedding plane within the same shale core. These shale cores, characterized by a dark black appearance and burial depths exceeding 2500 m, were extracted from shale reservoirs in the Chang 7 stratum of the Yanchang Formation in the Ordos Basin, China. Originating from the Late Triassic, this formation signifies a significant era of lacustrine basin development within the intracontinental depression of the Ordos Basin. It represents a typical rich in organic matter terrestrial shale. X-ray diffraction (XRD) analysis was utilized to quantify the primary mineral components, while total organic carbon was determined via rock pyrolysis analysis. Samples densities, determined using an Archimedean displacement method, had an approximate uncertainty of ±0.5%. Porosity was measured using a He pycnometer employing the particle volume method, with a relative error of less than 5%. Experimental results for the sample series (#B1–#B3 and #K1–#K3) are summarized in Table 1. In this study, quartz, calcium, and pyrite minerals were classified as brittle minerals, while clay is considered a non-brittle (ductile) mineral, consistent with previous studies (Wang and Gale, 2009; Xie et al., 2023). Analysis reveals that the #B series samples exhibit similar TOC content (approximately 10%, Table 1), with the total brittle minerals (quartz + calcium + pyrite) increasing from samples #B1 to #B3, and vice versa for the clay content. Scanning electron microscopy (SEM) observations illustrate that the #B series samples have a similar microstructure, where organic matter and clay exhibit an interbedded distribution (Fig. 2). The #K series samples exhibit complicated distribution for the microstructure of components. Notably, organic matter in the #K1 sample is mainly characterized by a pore-filling type (patchy) distribution in micropores, while in #K2 and #K3, the distribution of organic matter is both patchy pore-filling and stratified type (stripes) (Fig. 3).

The ultrasonic velocities of compressional waves (V_P) and shear waves (both V_{SV} and V_{SH}) were measured at different directions

Table 1
Mineral components and basic parameters for samples #B series and #K series (Q + C + F denotes quartz + calcium + pyrite).

No.	TOC, %	Clay, %	Quartz, %	Calcium, %	Pyrite, %	Brittle minerals (Q + C + F), %	Density, g/cm^3	Porosity, %
#B1	10.2	47.8	32.4	6.4	3.2	42.0	2.33	0.89
#B2	10.6	42.4	29.1	14.2	3.7	47.0	2.31	0.83
#B3	10.3	37.4	27.7	19.8	4.8	52.3	2.37	1.00
#K1	3.4	46.7	23.8	16.2	9.9	49.9	2.48	2.26
#K2	7.1	45.6	33.1	4.6	9.6	47.3	2.41	2.32
#K3	10.4	42.1	23.2	12.0	12.3	47.5	2.36	2.33

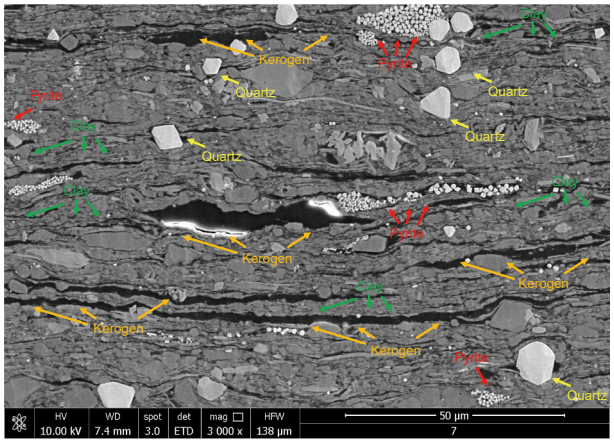

Fig. 2. SEM observations for the samples #B series.

(0°, 45°, 90°) for all samples using 0.5 MHz transducers. The velocities' anisotropic parameters were subsequently calculated and are presented in Table 2. Following the method suggested by Yin (1993), the relative errors of ultrasonic pulse transmission techniques were determined to be 0.7% and 1.2% for V_P and Vs measurements, respectively. Anisotropic tensile strengths, determined at different directions (0°, 45°, 90°) for all samples through Brazilian mechanical tests, was conducted using the MTS 815 hydraulic servo-control testing system at Chengdu University of Technology (Fig. 4). During the loading process, stress was applied with a constant loading rate of 200 N/s for all tests, following the ISRM standards towards failure (Bieniawski and Hawkes, 1978). It is noteworthy that the samples were cut into disk samples with a diameter of 25 mm and thickness of 5 mm for Brazilian splitting testing.

In the initial phase of the test, samples were meticulously positioned within a contoured fixture to ensure precise alignment of the loading line with the specified loading direction. Subsequently, the test rack was carefully placed onto the MTS 815 rock mechanics test system, administering gradual radial pressure to the specimens through a precision pressure servo mechanism. Throughout the testing procedure, the loading stress steadily and progressively escalated, while the pressure head continuously descended at a predefined rate until the juncture at which the specimen eventually experienced failure. The results of tensile strengths for the samples are presented in Table 3.

3.2. Optimization of anisotropic tensile strength criteria

The tensile strength anisotropy equation is a crucial component of the new brittle anisotropic model, enabling the comprehensive characterization of the directional variation of brittleness in both the elastic and fracture stages. Simultaneously, it effectively

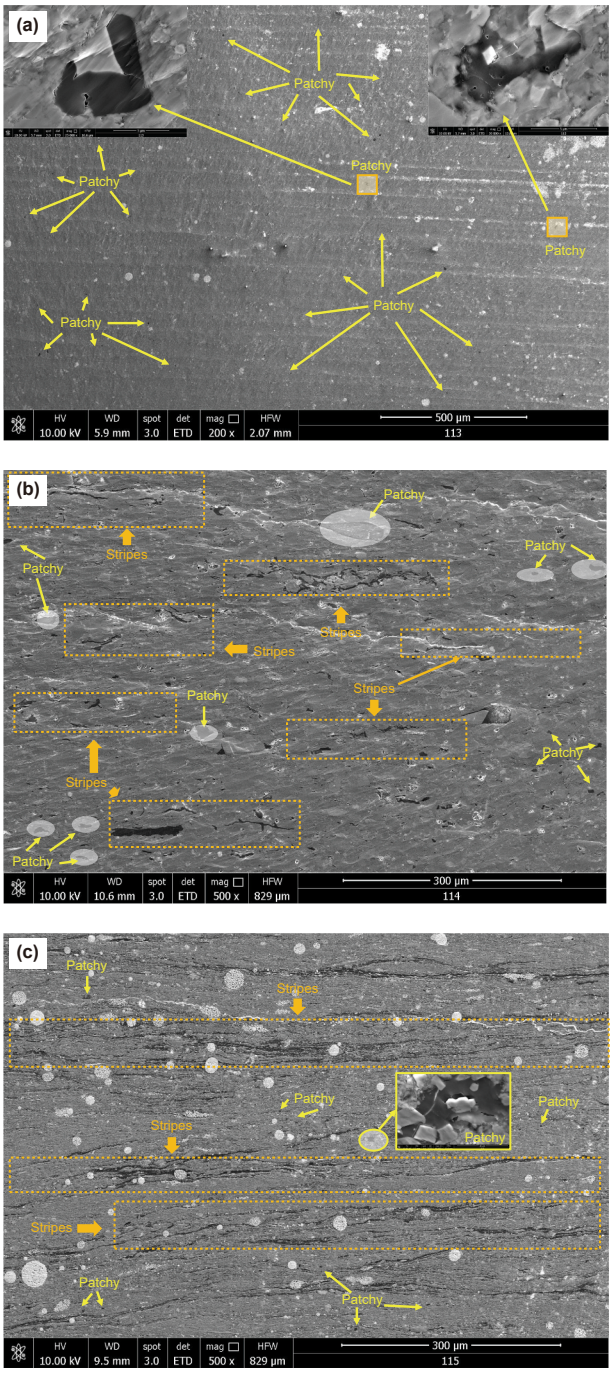

Fig. 3. SEM observations for the samples #B series: **(a)** sample #K1, organic matter is mainly characterized by a patchy (pore-filling type) distribution; **(b)** sample #K2, distribution of organic matter is both patchy pore-filling and striped type; **(c)** sample #K3, distribution of organic matter is both patchy pore-filling and striped type.

Table 2
Experimental measurements of the ultrasonic speeds at different directions (0°, 45°, 90°) and velocities anisotropic parameters of shale for samples #B and #K series.

No.	V_P (0°), m/s	V_P (45°), m/s	V_P (90°), m/s	V_{SV} (0°), m/s	V_S (45°), m/s	V_{SH} (90°), m/s	ε	γ
#B1	3048	3620	4377	1773	2251	2660	0.53	0.63
#B2	3367	3834	4359	2066	2369	2691	0.34	0.35
#B3	3681	4036	4542	2219	2526	2825	0.26	0.31
#K1	3520	4129	4928	2086	2563	2976	0.48	0.52
#K2	3215	3888	4703	1865	2274	2719	0.57	0.56
#K3	3380	3897	4620	2004	3400	2776	0.43	0.46

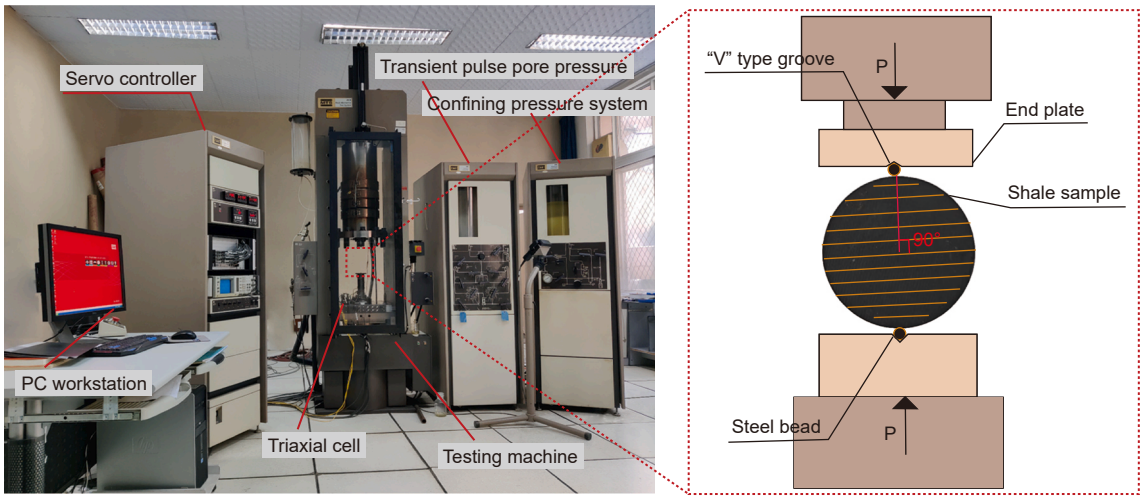

Fig. 4. MTS 815 mechanical and ultrasonic testing system at Chengdu University of Technology.

Table 3
The tensile strength at different directions (0°, 45°, 90°) for the samples #B and #K series.

Angle	Tensile strength, MPa					
	#B1	#B2	#B3	#K1	#K2	#K3
0°	5.69	6.16	6.86	6.76	6.05	6.33
45°	6.63	7.38	7.90	7.93	7.16	7.34
90°	8.23	8.09	8.65	9.56	8.85	8.78

addresses the limitation of traditional brittle anisotropic equations, which fail to avoid the issue of increased shale stiffness due to high Young's modulus, making it less prone to fracturing. Over the years, researches have conducted to theoretically characterizing tensile strength anisotropy. Jaeger (1960) initially proposed the single plane weakness criterion to describe tensile strength anisotropy theoretically. Through direct tensile experiments, Nova and Zaninetti (1990) discovered a close correlation between the variation in tensile strength and the loading angle, introducing the N-Z criterion for characterization. Lee and Pietruszczak (2015) assumed that every physical plane, except the weak plane, has the same tensile strength. Building on the SPW criterion, they derived the L-P criterion applicable to characterizing the directional variation of tensile strength in laminated rocks. Simultaneously, Lee and Pietruszczak (2015), using the critical plane method, utilized a second-order tensor representing directional deviations in tensile strength spatial distribution to derive the CPA criterion, characterizing tensile fracture in orthotropic media. Liu et al. (2022) introduced an anisotropic coefficient and proposed the P-Q criterion based on direct tensile experiments on slate samples. In order to further assess the applicability and accuracy of different criteria in characterizing the directional variation of tensile strength for the shale in the study area, the tensile strength test data from two shale groups, labeled as B and K, were input into various criteria. It is noteworthy that the theoretical curves of these criteria only require input data of tensile strength experiments in directions parallel and perpendicular to the bedding. Hence, the accuracy of predictions for different theories was verified using the tensile strength at nonsymmetric angles.

Fig. 5 presents the tensile strength test results alongside corresponding theoretical prediction curves for various loading directions in shale groups B and K. The results indicate that the N-Z criterion, LPA criterion, and CAP criterion all provide reasonably accurate predictions. To facilitate a more intuitive comparison of the predictive performance of these models, the relative errors between the measured tensile strengths and the theoretical predictions were calculated for samples cored at 45° (Fig. 6). Colored dashed lines in the figure represent the relative errors associated with each theoretical model. Comparative analysis shows that the N-Z criterion delivers the highest predictive accuracy—most notably for the K-series samples, where the predicted curve closely aligns with experimental data. For these samples, the relative error is consistently within 1%, significantly outperforming the other models. While the CPA, LPA, and N-Z criteria all achieve relative errors within 5% for the B-series samples, the N-Z criterion exhibits both superior accuracy and greater stability across sample groups. This performance is the key reason the N-Z criterion was selected as the foundation for the anisotropic brittleness model developed in this study. The comparatively higher prediction error of the N-Z model for the B-series samples (Fig. 6) is attributed to their more complex microstructural anisotropy. These samples feature dense skeletal organic matter (OM) bands and irregular mineral–OM interfaces, which disrupt the continuity of bedding-parallel fracture paths and introduce localized anisotropy beyond the assumptions of vertical transverse isotropy (VTI). In contrast, the K-series samples display more regular lamination and OM

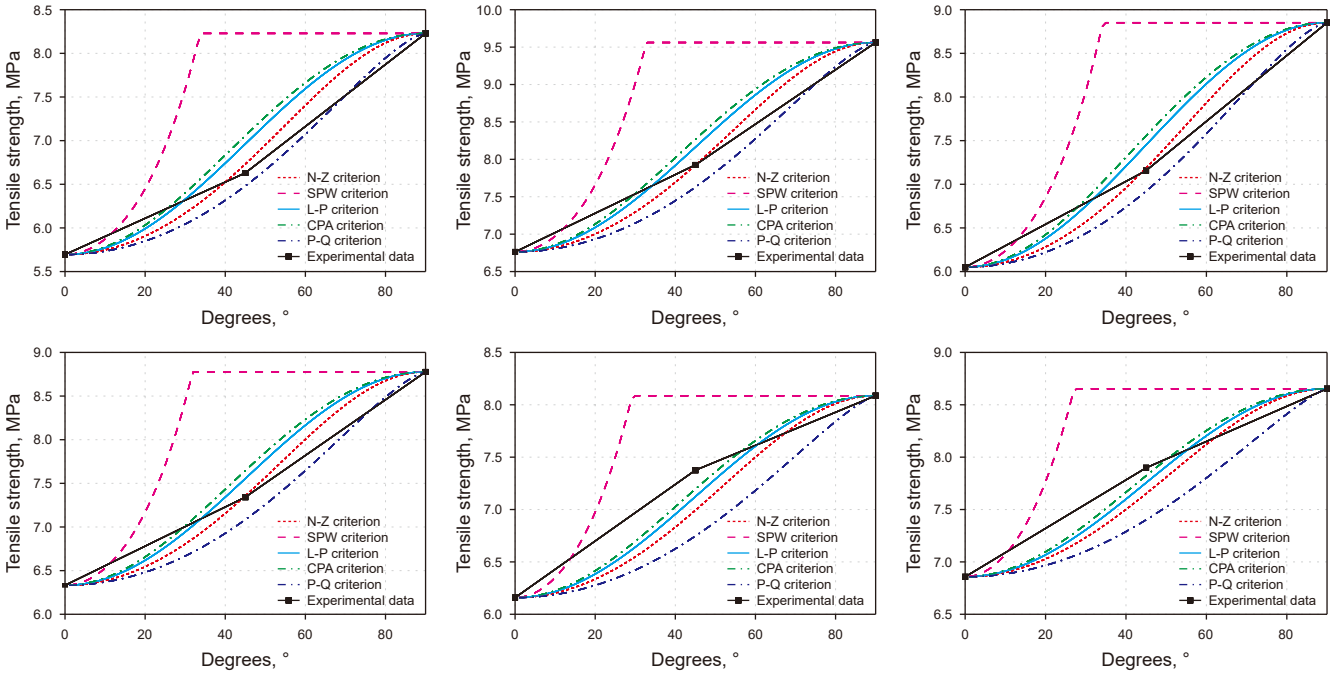

Fig. 5. Experimental measurements (0°, 45°, 90°) and predicted curves of anisotropic tensile strength by different theoretical criterions (SPW criterion, N-Z criterion, L-P criterion, CPA criterion and L-P criterion).

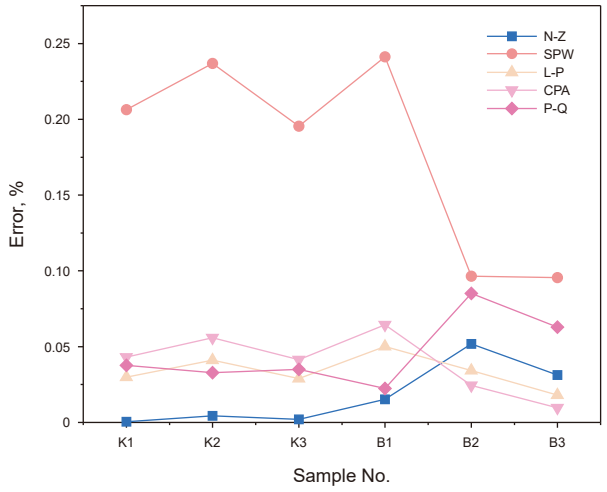

Fig. 6. Comparison of experimentally measured tensile strength with predictions from the SPW, CPA, L-P, P-Q and N-Z criteria. The SPW model fails to capture the observed weakening at oblique angles due to its assumption of a discrete weak plane. CPA offers improved orientation prediction but underestimates anisotropic strength variation due to idealized tensor symmetry. The N-Z criterion closely matches the observed strength profile across all orientations.

morphology, resulting in greater directional coherence and improved agreement between theoretical predictions and experimental results.

3.3. Validation of the quantitative anisotropic brittleness model

Based on the comparison and error analysis of the tensile strength anisotropy theoretical prediction curves and experimental test values, the N-Z criterion was identified as suitable for characterizing the directional variation of tensile strength in lacustrine shale. By incorporating this expression into Eq. (1), the new brittle anisotropic theoretical model can be determined. The next step involves experimental validation of the new model. Whole-rock analysis test results indicate that the organic matter content of the #B series samples is roughly equivalent, while the content of brittle minerals gradually increases from B1 to B3, with a corresponding decrease in the content of ductile minerals (mainly clay) (Table 1). Additionally, scanning electron microscope microstructure images (Fig. 2) reveal that in the #B series samples, brittle minerals (such as quartz) predominantly exhibit isotropic granular shapes, while the bedding structure is mainly composed of interlayered clay and organic matter. In situations where content and structures of the organic matter is similar (e.g. #B series samples), both brittle minerals and layered clay minerals act as matrix skeletons of the rock, providing support and undergoing stress, thereby influencing the brittleness characteristics of the samples. At this point, the brittleness characteristics show a positive correlation with brittle minerals represented by quartz, while ductile minerals represented by clay exhibit a negative correlation with brittleness characteristics. Therefore, for the #B series samples, the predicted brittleness values in any given direction should gradually decrease from B1 to B3.

By incorporating the velocity anisotropy test data and tensile strength anisotropy test data for the #B series samples from Tables 2 and 3 into the new brittle theoretical model, the predicted curves for the directional variation of brittleness characteristics for the corresponding three sets of samples can be calculated (Fig. 7). The results indicate that all three sets of samples exhibit varying degrees of directional brittleness characteristics. In the range of 0°–180°, perpendicular to the bedding, the brittleness values first increase and then decrease, reaching the maximum in the parallel bedding direction and the minimum in the perpendicular bedding direction. The entire curve is approximately symmetrical about the bedding direction. The results in Fig. 6 show that within the range of 0°–360°, brittleness values corresponding to the same angle are positively correlated with the content of brittle minerals and negatively correlated with the

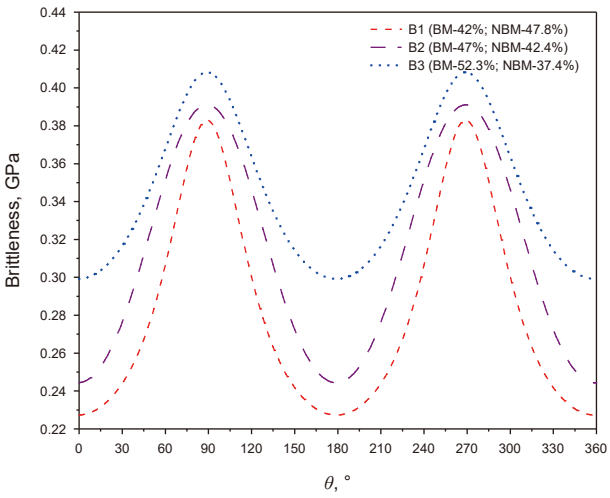

Fig. 7. Predicted curves for the directional variation of brittleness characteristics by the new brittleness anisotropic model for samples #B series. BM denotes brittle minerals, and NBM denotes the non-brittle minerals.

content of plastic minerals. This is consistent with the previous analytical results, demonstrating the accuracy of the new brittleness model to some extent. Furthermore, based on the theoretical prediction curves, the brittleness anisotropy values for the three sets of samples were calculated ($(|B(//) - B(\perp)|/B(//)) \times 100\%$) (Fig. 8). The vertical axis for the left side of the graph represents different-numbered samples in the #B series, the horizontal axis represents different mineral component contents, and the different-colored rectangles represent different mineral proportions. Red represents brittle minerals, blue represents clay mineral proportions, and light blue represents organic matter proportions. It is easily observed that from B1 to B3, the content of brittle minerals gradually increases, while clay minerals decrease, and the organic matter content remains roughly constant. The right side of Fig. 8 represents different sample numbers on the vertical axis, the lower horizontal axis represents velocity anisotropy values, and the upper horizontal axis represents brittleness anisotropy values (ΔB). The results show that from B1 to B3, the clay content decreases from 47.77% to 37.43%, and the corresponding brittleness anisotropy value decreases from 40.64% to 26.71%, demonstrating a strong positive correlation between ΔB and clay content. As mentioned earlier, the bedding characteristics of the #B series samples are mainly controlled by the interlayered structure of clay and organic matter. With the organic matter content being relatively constant, the content of layered clay becomes the main controlling factor of bedding structure characteristics. Based on the causal relationship between rock elastic and mechanical anisotropy and bedding structure, the #B series samples demonstrate that increasing the content of layered clay enhances bedding development, thereby amplifying directional brittleness. As a result, a positive correlation is observed between clay content and the brittleness anisotropy index ΔB, which aligns well with the ΔB trends calculated using the proposed anisotropic brittleness model across the three shale samples. This consistency supports the validity and applicability of the model in capturing shale brittleness behavior. Notably, a gradual decrease in compressional and shear wave velocity anisotropy is observed from samples B1 to B3 (Table 2 and Fig. 8). This trend is likely attributable to the weakening of bedding-related anisotropy, which in turn correlates with a reduction in layered clay content. These observations reinforce the causal link between bedding structure and elastic anisotropy, further validating the physical basis of the model.

4. Effect of TOC on brittleness anisotropy based on the proposed model

The results of previous studies indicate that the brittleness characteristics of shale and their directional variations are influenced not only by the type and content of mineral components (e.g., an increase in the content of brittle minerals, represented by quartz, strengthens the brittleness response of rocks, while plastic minerals, represented by clay, weaken the brittleness characteristics of rocks) but also by the spatial distribution of minerals. For instance, an increase in the layered distribution of clay enhances the brittleness anisotropy characteristics. As an integral component shaping the intricate matrix of shale rocks, kerogen is considered a crucial variable determining both elastic and mechanical properties. Recent quantitative experiments in rock

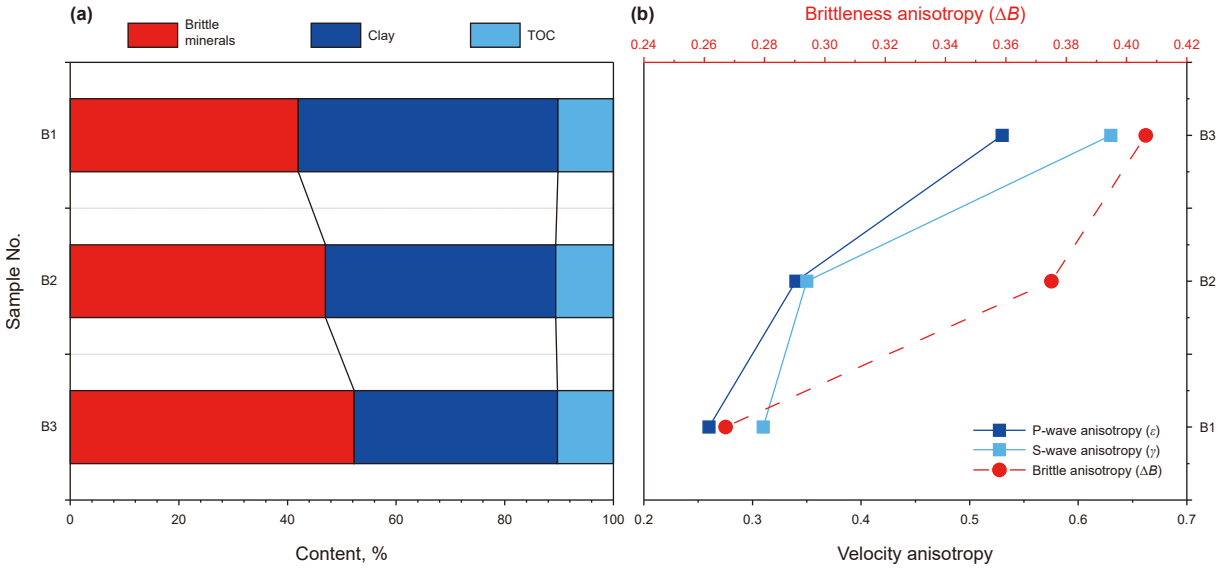

Fig. 8. Mineral components **(a)** and evaluation result **(b)** of the proposed quantitative brittleness model for the samples #B series.

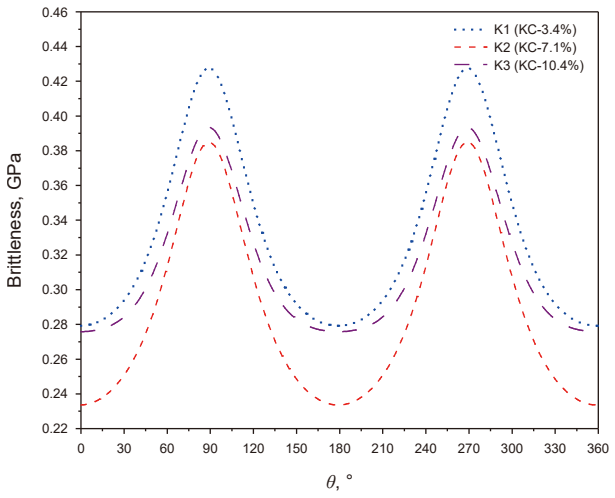

Fig. 9. Predicted curves for the directional variation of brittleness characteristics by the new brittleness anisotropic model for samples #K series. KC denotes kerogen content.

physics have shown that, under similar microscopic structural distributions, the kerogen content is negatively correlated with shale brittleness characteristics (Xie et al., 2023). However, for lacustrine shale, not only does kerogen content vary significantly, but its occurrence forms and microscopic structural distribution also differ considerably (Figs. 2 and 3). Therefore, it is crucial to investigate how the brittleness characteristics of lacustrine shale are affected by different microscopic structural distributions of kerogen and its content. However, there is scarce literature addressing these issues, especially regarding the unclear impact and response mechanisms of kerogen content and structure on the directional brittleness variations.

Thus, based on the new brittleness anisotropy theoretical model, combined with the acoustic and mechanical test results of the #K series shale samples (Tables 2 and 3), predictive curves for the directional variations in brittleness for the three samples can be obtained (Fig. 9). The results show that the #K series samples all exhibit significant brittle anisotropy characteristics. Within the range of 0°–180° perpendicular to the bedding, the brittleness values first increase and then decrease, reaching the maximum in the parallel bedding direction and the minimum in the perpendicular bedding direction, and the entire curve is approximately symmetrical about the bedding direction. The results depicted in Fig. 8 reveal a discernible trend in the brittleness values corresponding to identical angles as the total organic carbon (TOC) content increases. Specifically, these values exhibit an initial decrease followed by a subsequent increase, and across the entire 0°–360° range relative to the bedding direction, the brittleness values corresponding to any given angle demonstrate a consistent pattern of variation. Additionally, based on the theoretical prediction curves in Fig. 8, the brittleness anisotropy values ((|B(Parallel) − B(Perpendicular)|/B(Parallel)) × 100%) for the three sets of samples were calculated. Combining velocity anisotropy theory (Thomsen, 1986) and longitudinal and transverse wave velocity test results in different directions, the anisotropy values (ε and γ) for the three sets of samples were calculated. As shown in Fig. 9, the vertical axis on the left side represents different sample numbers in the #K series, while the horizontal axis represents the content of different mineral components. The lengths of the rectangles of different colors represent the proportions of different minerals. Among them, red represents the proportion of brittle minerals, blue represents the proportion of clay minerals, and light blue represents the organic matter content. The right side of Fig. 10, the vertical axis represents different sample numbers, the bottom horizontal axis represents velocity anisotropy parameters (ε and γ), and the top horizontal axis represents brittle anisotropy values (ΔB). it shows that from K1 to K3, ε, γ, and ΔB all exhibit a trend of first increasing and then decreasing. These predictions contradict numerous earlier studies that indicated TOC is a mechanically weak mineral and negatively correlates with rock brittleness (Wang and Gale, 2009; Rybacki et al., 2016; Xie et al., 2023). One key reason is that exploring the correlation between the brittleness or directional variations in brittleness and TOC of lacustrine shale not only requires considering the influence of content but also the impact of its microscopic structural distribution, a factor often overlooked in previous research.

In fact, earlier scanning electron microscopy observations were conducted for the #K series samples (Fig. 3). The clay in all three samples exhibits a distinct layered distribution feature, and brittle

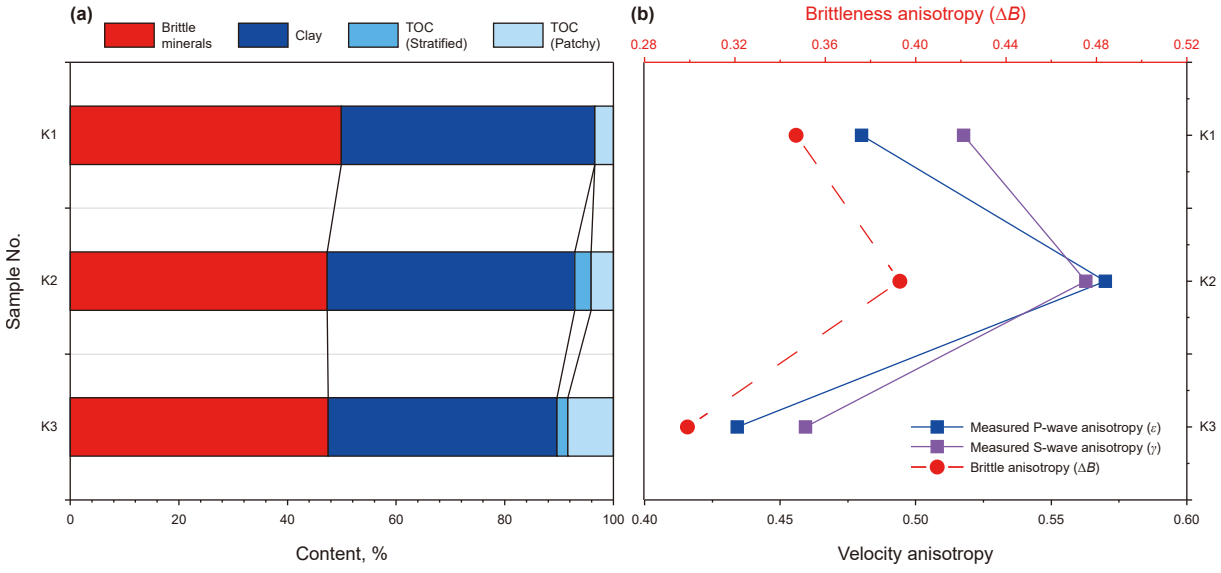

Fig. 10. Mineral components **(a)** and evaluation result **(b)** of the proposed quantitative brittleness model for the samples #K series.

minerals (such as quartz) mostly display a granular distribution, while the structural distribution of TOC is more complex. In the #K1 sample, most organic matter fills the pores in a patchy structure (Fig. 3(a)), exhibiting isotropic characteristics and does not contribute to skeletal support, the brittleness value is primarily controlled by the presence of brittle minerals and clay minerals in the rock matrix, showing a positive correlation with the content of brittle minerals, while negatively correlated with clay content when the content of brittle minerals is constant. Meanwhile, the strength of brittle anisotropy is mainly controlled by the content of laminated clay minerals. In contrast, in addition to patchy pore-filling TOC, the K2 and K3 samples also contain striped organic matter (Fig. 3(b) and (c)), which contributes to skeletal support. Studies have shown that when organic matter serves as a rock framework, it acts as a mechanically weak mineral, and an increase in this type of organic matter will weaken rock brittleness, consistent with previous research conclusions. Interestingly noted that the striped organic matter is often interlayered with clay (Fig. 3(b) and (c)). In this context, the brittleness value of the K2 and K3 sample is jointly controlled by the brittle minerals, striped organic matter, and clay minerals in the framework. Specifically, brittleness strength exhibits a negative correlation with the combined content of striped organic matter and clay minerals, and a positive correlation with the proportion of brittle minerals. In contrast, the degree of brittleness anisotropy is primarily governed by the total content of striped organic matter and clay. Clarifying the quantitative relationships among brittleness strength, brittleness anisotropy, and their dominant controlling factors not only provides a robust explanation for the predictions made by the proposed theoretical model but also sheds light on the underlying micromechanical mechanisms driving these relationships. Subsequent sections will offer a more in-depth analysis based on rock physics modeling using effective medium theory. It is important to note that although the B-series samples have higher TOC values, the K-series samples were chosen for evaluating the influence of organic matter on brittleness anisotropy due to their greater microstructural diversity. Specifically, the K1 and K2 subgroups feature pore-filling and striped skeletal organic matter, respectively, allowing for a controlled comparison of OM morphology and its effect on mechanical anisotropy.

5. Discussion

5.1. Elastic anisotropy and tensile fracture mechanism

At the micromechanical level, brittle failure in shale is governed by a combination of factors: (1) mineral composition and grain packing; (2) the mechanical contrast and bonding strength between different mineral phases (e.g., quartz vs. clay); (3) the geometry and continuity of bedding-parallel weak planes; and (4) the distribution and role of organic matter, particularly whether it acts as a passive pore-filling phase or a load-bearing skeletal framework. For example, in directions perpendicular to bedding, cracks may be arrested by stiff, isotropic brittle minerals, while in directions oblique to bedding, interbedded layers of clay and striped OM may localize strain and promote tensile fracture. These micromechanical contrasts lead to directional differences in both elastic wave propagation and tensile failure resistance.

Microscale observations show that elastic stiffening does not necessarily equate to reduced tensile weakness, particularly in organic-rich shales where skeletal-type organic matter (OM) is interbedded with clay. High-resolution SEM imagery and XRD data from the Chang 7 shale samples reveal that skeletal OM forms elongate, aligned structures that participate in the mechanical framework of the rock (Figs. 2 and 3, Table 1). These OM-rich bands often coincide with laminar clay-rich zones, creating mechanically anisotropic layering with significant directional contrast in both stiffness and cohesion. Although the quartz framework may provide elevated elastic stiffness (e.g., higher E along bedding planes), the skeletal OM–clay interfaces often serve as preferred zones for crack nucleation under tensile stress. This decoupling between stiffness and fracture resistance is especially pronounced in orientations oblique to bedding, where tensile strength is lowest despite moderate or high elastic moduli. Therefore, stiff elastic response at the macroscale can coexist with structurally weak, failure-prone paths at the microscale—underscoring the importance of integrating elastic and fracture criteria in brittleness modeling. By integrating both stiffness-driven and failure-driven mechanisms, our model captures this inherent anisotropy in shale brittleness and avoids overestimating brittleness in stiff but fracture-resistant directions. This mechanistic coupling also enhances the physical realism and predictive capability of the model for applications in fracture design and sweet-spot evaluation.

To further illustrate the underlying mechanism of the proposed model, a schematic diagram (Fig. 11) has been introduced to visualize how elastic anisotropy and tensile fracture anisotropy jointly determine directional variations in shale brittleness. As shown in the left panel of Fig. 11, elastic anisotropy manifests as directional variation in both Young's modulus and Poisson's ratio, governed by the orientation of mineral alignments and bedding structures. In transversely isotropic shale, $E(\theta)$ typically peaks parallel to bedding (90°), while $\nu(\theta)$ reaches a minimum along the same direction. This implies that under uniaxial loading, elastic stiffness is highest in the horizontal direction. However, fracture initiation is not solely controlled by stiffness. The right panel displays tensile strength anisotropy $T(\theta)$, which tends to be lowest at oblique angles (e.g., 30°–60°), where bedding-parallel weak planes such as clay or striped organic matter facilitate tensile crack propagation. These trends are captured using the Nova–Zaninetti (N-Z) criterion. The center of Fig. 4(a) combines these mechanisms: brittleness is highest in directions where elastic energy can be efficiently stored ($E\uparrow$) and tensile resistance is weakest ($T\downarrow$). The 3D shale block highlights how fracture development is favored when these two conditions spatially coincide. Thus, the proposed model accounts for both pre-failure mechanical response and

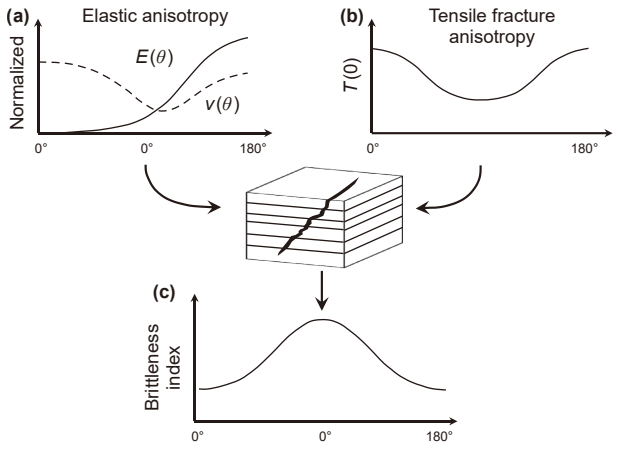

Fig. 11. Schematic diagram illustrating how elastic anisotropy and tensile fracture jointly influence shale brittleness. **(a)** Directional variation in elastic parameters (Young's modulus $E(\theta)$ and Poisson's ratio $\nu(\theta)$); **(b)** anisotropic tensile strength $T(\theta)$, based on the N-Z criterion; **(c)** central panel integrates these into a composite brittleness index $B(\theta) = B_E(\theta)/T(\theta)$. A conceptual shale block in the center visualizes bedding structure and directionally preferred fracture planes. Arrows emphasize that high stiffness (E) and low tensile strength (T) must align for brittleness to peak.

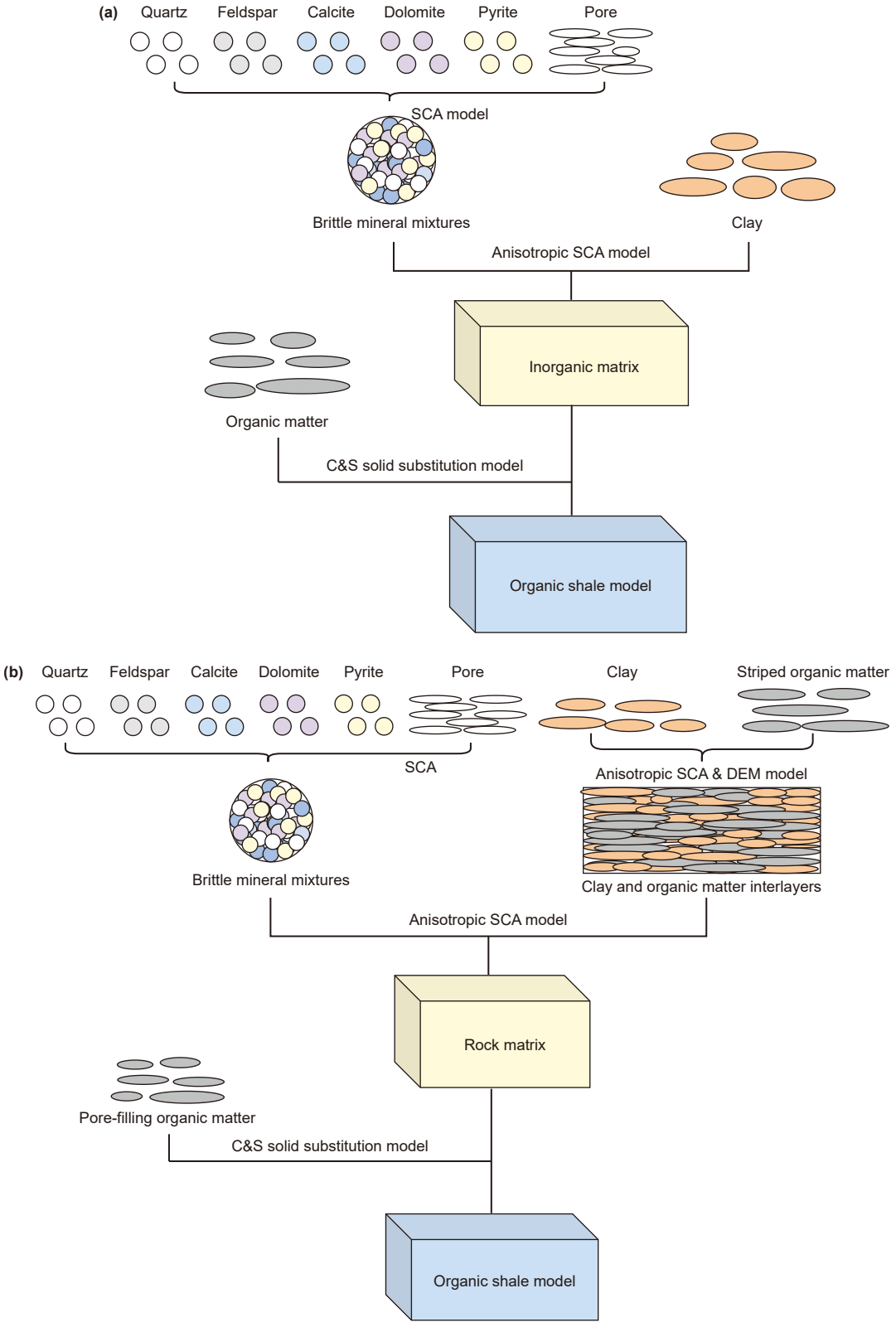

Fig. 12. Workflow of the rock physical models for sample #K series. **(a)** Sample #K1, the organic matter is mainly characterized by a patchy pore-filling distribution and can be treated as a filling material of the inclusion space instead of the load-bearing matrix; **(b)** samples #K2 and #K3, the organic matters are characterized by both patched pore-filling and striped distributions.

Table 4
Results of the velocities anisotropic parameters from experimental measurements and rock physical modeling predictions.

No.	Measured ε	Predicted ε	Measured γ	Predicted γ
#K1	0.480	0.456	0.518	0.524
#K2	0.570	0.536	0.563	0.566
#K3	0.430	0.431	0.460	0.463

Table 5
Components of the organic matter with different microstructures (Pore-filling and Stratified type) determined by rock physical modeling prediction.

No.	Clay content	TOC content	Pore-filling TOC	Stratified TOC	Clay & Stratified TOC
#K1	46.7%	3.4%	3.4%	0	46.7%
#K2	45.6%	7.1%	4.1%	3%	48.6%
#K3	42.1%	10.4%	8.4%	2%	44.1%

post-failure tensile rupture behavior, providing a more comprehensive and physically grounded framework for brittleness evaluation in anisotropic shale reservoirs.

5.2. Mechanism on the organic matter and brittleness anisotropic behaviors

To further elucidate the relationship between the organic matter and brittleness anisotropic behaviors and clarify the corresponding response mechanism, rock physics models (RPM) were developed based on the compositional characteristics and microscopic structural distribution features of the #K series samples (Fig. 3 and Table 1). Specifically, For Sample #K1, the self-consistent model (SCA, Berryman, 1995) is firstly used to form a spatial combination of brittle mineral mixtures (quartz + feldspar + calcite + pyrite), then we use anisotropic SCA (Hornby et al., 1994) to include brittle mineral mixtures in the fully aligned clay to obtain the effective anisotropic elastic stiffness of inorganic matrix (Zhao et al., 2016). Based on the observations in Fig. 3(a), the organic matter is mainly characterized by a patchy pore-filling distribution and can be treated as a filling material of the inclusion space instead of the load-bearing matrix. In this sense, the C&S solid substitution equation (Ciz and Shapiro, 2007) is used to modeling the combined effect of the organic-matter on the overall elastic properties of organic shale, the workflow of rock physical model for sample #K1 is shown in Fig. 12(a). For samples #K2 and #K3, both pore-filling and striped organic matter can be observed simultaneously from Fig. 3(b) and (c). Among them, the striped organic matter intercalates with clay minerals to form interlayers, serving as a supportive framework, an anisotropic SCA + DEM model (Qian et al., 2020) was used to mix layered clay and striped organic matter to form a clay-organic matter mixture model. Following with the brittle mineral mixtures by the SCA model, the clay-organic matter intercalation mixture was combined with brittle mineral mixtures using an anisotropic SCA model to obtain the rock matrix framework. Finally, the pore-filling organic matter was incorporated into the matrix using C&S model, the workflow of rock physical model for sample #K1 is shown in Fig. 12(b). Based on the workflow of the proposed rock physical models and experimental inputs (Table 1), the Thomsen anisotropic parameters (ε and γ) can be calculated for the #K series samples (see Table 4). Subsequently, these simulated outcomes were projected onto the right half of Fig. 10, where it can be observed that the experimental test results and the model prediction results are in good agreement (Fig. 13), the coefficients of determination (R^2) for both predicted and measured P-wave and S-wave anisotropic parameters exceed 95%. On the one hand, this confirms the correctness of the RPM workflow and verifies the necessity of considering both type and content of organic matter in the modeling process. On the other hand, we can inversely calculate the content of various structured organic matter corresponding to the three samples based on the RPM (Table 5). In sample #K2, the pore-filling and striped organic matter account for 4.1% and 3%, respectively. In sample #K3, the corresponding proportions are 8.4% and 2%. Based on the discussed cause-and-effect relationship between brittleness strength and the variation of brittleness anisotropy with mineral compositions in the #K series samples: the content of brittle minerals in samples #K1 to #K3 first decreases and then increases (Table 1). Among them, sample #K1 has the highest content of brittle minerals (49.6%), so the brittleness strength of the #K series samples in the same

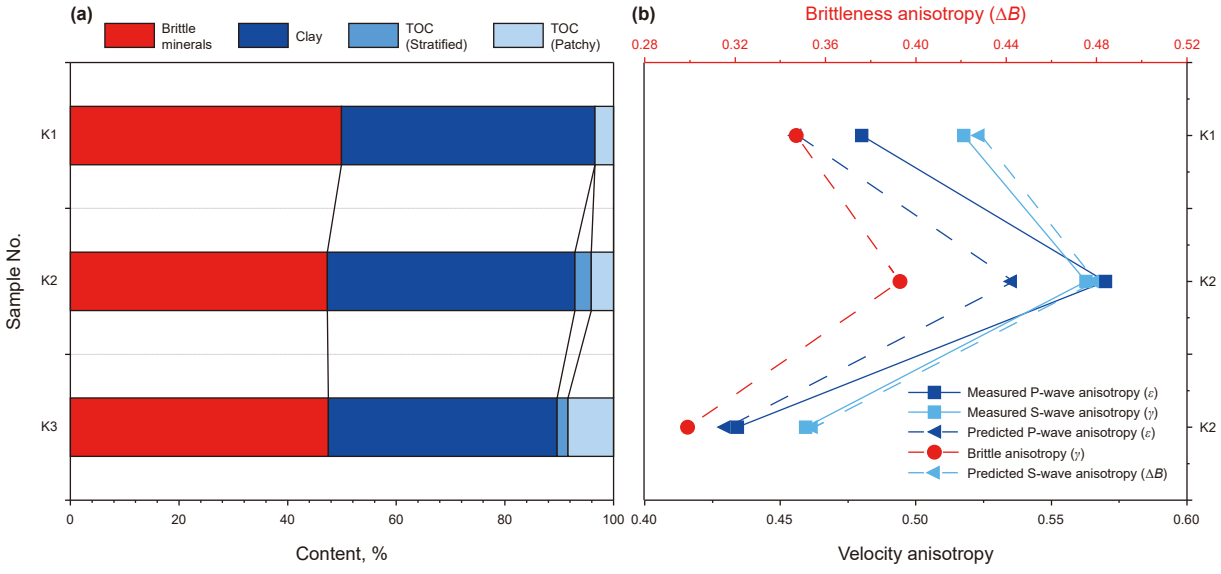

Fig. 13. The predicted velocities anisotropic parameters (ε, γ) by rock physical models and experimental measurements, and it shows a good agreement both for P-wave and S-wave anisotropic parameters.

direction also decreases first and then increases. Sample #K1 also exhibits the strongest brittleness characteristics, which align well with the predictions of the new brittleness evaluation model theory (Fig. 8). Striped skeletal support-type OM forms aligned, continuous bands that participate in the mechanical framework of the rock, often interbedded with clay. These layers act as mechanically weak planes with low stiffness and cohesion, promoting tensile failure and reducing overall brittleness. In contrast, pore-filling OM is discontinuous and plays a limited role in load transfer or crack propagation. As a result, skeletal OM reduces both the directional tensile strength and elastic modulus anisotropy, thereby weakening brittleness relative to pore-filling configurations.

Based on the results of rock physics modeling calculations, a ternary plot of Thomsen parameters (ε, γ) and brittle anisotropy value (ΔB) against the total content of striped organic matter and clay minerals can be obtained for the three samples (Fig. 14). It can be observed that ε, γ, and ΔB are all positively correlated with the total content of striped organic matter and clay minerals. This confirms the previous discussion that both velocity and brittleness anisotropy are primarily controlled by the content of striped organic matter and clay minerals. It also further explains the induced mechanism of the changing pattern of brittleness anisotropy values from increasing to decreasing from sample #K1 to #K3, corresponding to the increase and then decrease in the total content of striped organic matter and clay minerals (Table 5). Among them, sample #K3 has the lowest content of striped organic matter and clay minerals (44.1%). This is consistent with the conclusions predicted based on scanning electron microscopy observations mentioned earlier and demonstrates good consistency with the results predicted by the new brittleness evaluation model. It should be noted that while this model assumes vertical transverse isotropy (VTI) to characterize the anisotropic behavior of laminated shales, deviations from this assumption may arise in naturally fractured or tectonically deformed formations. Such deviations introduce orthotropy or even more complex anisotropic symmetry classes, which can significantly affect the directional distribution of stiffness and tensile failure. While the VTI assumption remains valid for the Chang 7 shale due to its well-preserved laminar structure and minimal natural fracturing, further extension of the model to orthotropic or fracture-dominated media is warranted in future studies to improve prediction accuracy in more heterogeneous reservoirs.

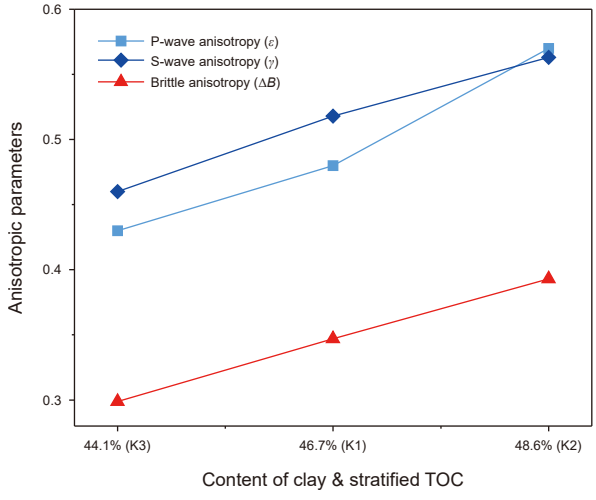

Fig. 14. Crossplot of anisotropic parameters (ε, γ and ΔB) and the total content of clay and stratified TOC.

6. Conclusion

This study presents a novel theoretical model for evaluating brittleness anisotropy in terrestrial shale, integrating elastic response characteristics with shear–tensile fracture mechanisms. The model effectively reconciles the traditionally observed contradiction between high Young's modulus and the actual tendency for brittle failure. Comparative analysis of quantitative rock physics data supports the integration of the Nova–Zaninetti (N-Z) criterion into the brittleness anisotropy framework, enhancing its theoretical robustness. Notably, the deviation between N-Z model predictions and measured tensile strengths remains below 5%, affirming the model's predictive accuracy. The proposed model reliably captures both the magnitude and directional variation of brittleness in response to differences in mineral composition, structure, and abundance. Specifically, brittleness values at a given orientation show a positive correlation with brittle mineral content and a negative correlation with plastic minerals. Clay content demonstrates a clear positive relationship with brittleness anisotropy. Interestingly, contrary to conventional assumptions, neither brittleness strength nor its anisotropy decreases monotonically with increasing organic matter content. Instead, brittleness behavior is governed by a combination of mineral composition and subtle variations in microstructural distribution. Isotropic brittle minerals emerge as the primary positive control on brittleness strength, whereas ductile components—particularly striped skeletal organic matter and clay—exert a secondary but significant weakening effect. In contrast, pore-filling organic matter contributes minimally to brittleness characteristics. Furthermore, the study highlights analogous patterns in velocity anisotropy, reinforcing the observed mechanical trends. Rock physics modeling of shale samples containing pore-filling OM alone and those with both pore-filling and striped skeletal OM further corroborates the mechanistic basis for the observed brittleness variations. In summary, the findings of this study provide a comprehensive theoretical and empirical foundation for the identification, evaluation, and optimization of hydraulic fracturing strategies in shale hydrocarbon reservoirs.

CRediT authorship contribution statement

Jian-Yong Xie: Writing – review & editing, Writing – original draft, Supervision, Methodology, Investigation, Funding acquisition, Conceptualization. **Yan-Ping Fang:** Writing – original draft, Validation, Investigation, Conceptualization. **Chun-Wei Wu:** Validation, Investigation. **She-Bao Jiao:** Resources, Validation. **Jing-Xiao Wang:** Validation, Supervision, Resources, Conceptualization. **Ji-Xin Deng:** Supervision, Resources. **Xing-Jian Wang:** Investigation, Methodology.

Declaration of competing interest

The authors declare that they have no known competing financial interests or personal relationships that could have appeared to influence the work reported in this paper.

Acknowledgements

This research is supported by the National Natural Science Foundation of China (42274175), Sichuan Provincial Joint Fund Project for Science, Technology and Education (2025NSFSC2035), Innovative Experimental Project at Institutions of Higher Education in Sichuan Province (Advanced Quantitative Rock Physics Investigations on the "Acoustic, Electrical, and Mechanical" Characteristics of Unconventional Reservoirs Subjected to Extreme

High Temperature and High Pressure Environments). The data or code relating to this work are available by contacting the corresponding author.

APPENDIX

(A) Self-consistent approximation (SCA) model

The self-consistent approximation model strategically positions the multiphase medium within an infinite matrix, fine-tuning the elastic parameters of this matrix to align seamlessly with those of the embedded multiphase media. Building upon this foundation, Berryman (1980, 1995) presented a versatile and comprehensive form of self-compatible approximation for N-phase mixtures, offering a robust framework for analyzing complex multiphase systems.

$$\begin{aligned}\sum_{i=1}^{N} x_i(K_i - K_{sc}^*)P^{*i} = 0\\ \sum_{i=1}^{N} x_i(u_i - u_{sc}^*)Q^{*i} = 0\end{aligned} \tag{A.1}$$

where i refers to the i-th inclusion material, x_i is the volume fraction of the i-th inclusion, K_i is the bulk modulus of the i-th inclusion, u_i is the shear modulus of the i-th inclusion, K_{sc}^* is the self-compatible bulk modulus of a multiphase mixture, u_{sc}^* is the self-compatible shear modulus of a multiphase mixture, P and Q are the form factors, the superscript $*i$ of P and Q refers to the fact that this form factor is for the inclusion material i of the background medium with a self-compatible equivalent modulus of K_{sc}^* and u_{sc}^*.

Anisotropic self-consistent approximation (SCA) model is showed as below:

$$\begin{aligned}\underset{\sim}{\boldsymbol{C}}^{sca} = \sum_{n=1}^{N} v_n \underset{\sim}{\boldsymbol{C}}^n \left(\underset{\sim}{\boldsymbol{I}} + \boldsymbol{G}^{\wedge}\left(\underset{\sim}{\boldsymbol{C}}^n - \underset{\sim}{\boldsymbol{C}}^{sca}\right)\right)^{-1}\\ \left\{\sum_{p=1}^{N} v_p \left(\underset{\sim}{\boldsymbol{I}} + \boldsymbol{G}^{\wedge}\left(\underset{\sim}{\boldsymbol{C}}^p - \underset{\sim}{\boldsymbol{C}}^{sca}\right)\right)^{-1}\right\}^{-1}\end{aligned} \tag{A.2}$$

$$\overset{\wedge}{\boldsymbol{G}}_{ijkl} = \frac{1}{8\pi}\left(\bar{\boldsymbol{G}}_{ikjl} + \bar{\boldsymbol{G}}_{jkil}\right)$$

where the tensor $\boldsymbol{G}$ serves as the Eshelby tensor, overseeing the shape of each individual inclusion. Furthermore, the symbol $\boldsymbol{I}$ represents the identity tensor, whereas $\underset{\sim}{\boldsymbol{C}}^n$ signifies the stiffness matrix pertaining to the n-th phase material, and v_n denotes its corresponding volume fraction.

(B) Anisotropic differential effective-medium (DEM) model

The differential effective-medium model (DEM) serves as a potent tool for modeling two-phase mixtures. This approach assumes the presence of a solid mineral phase constituting the volume of the rock matrix, upon which an inclusion phase of a specified volume is introduced. Subsequently, the mineral phase of equivalent volume (ΔV) is replaced by the inclusion phase, resulting in a transformation of the original rock matrix into a homogeneous medium. This medium is characterized by the equivalent elastic modulus of the newly formed composite. This process is iteratively repeated until the desired volume ratio between the solid mineral phase and the contained inclusion phase is achieved.

The system of coupled differential equations for the equivalent bulk modulus and shear modulus is (Berryman, 1992):

$$\begin{aligned}(1-y)\frac{\mathrm{d}}{\mathrm{d}y}[K^*(y)] = (K_2 - K^*)P^{(*2)}(y)\\ (1-y)\frac{\mathrm{d}}{\mathrm{d}y}[u^*(y)] = (u_2 - u^*)Q^{(*2)}(y)\end{aligned} \tag{B.1}$$

The initial conditions are $K^*(0) = K_1$ and $u^*(0) = u_1$, where K_1, u_1 are the bulk modulus and shear modulus of the initial main phase material (phase 1), K_2, u_2 are the bulk modulus and shear modulus of the gradually added inclusions (phase 2), y is the content of phase 2. For fluid inclusions and empty inclusions, y is equal to porosity ϕ. P and Q are the geometric factors of the shape, and the superscript *2 refers to the geometric factor for the inclusion material 2 in the background medium with equivalent modulus K^* and u^*.

Hornby et al. (1994) gave the expression for anisotropic DEM:

$$\begin{aligned}\frac{\mathrm{d}}{\mathrm{d}V}\left(\boldsymbol{C}^{\mathrm{DEM}}(V)\right) = \frac{1}{1-V}\\ \left(\boldsymbol{C}^i - \boldsymbol{C}^{\mathrm{DEM}}(V)\right)\left[\boldsymbol{I} + \widehat{\boldsymbol{G}}\left(\boldsymbol{C}^i - \boldsymbol{C}^{\mathrm{DEM}}(V)\right)\right]^{-1}\end{aligned} \tag{B.2}$$

$$\widehat{\boldsymbol{G}}_{ijkl} = \frac{1}{8\pi}\left(\bar{\boldsymbol{G}}_{ikjl} + \bar{\boldsymbol{G}}_{jkil}\right) \tag{B.3}$$

where $\boldsymbol{C}^{\mathrm{DEM}}$ represents the equivalent medium stiffness tensor obtained by the DEM method, V is volume of a material, $\boldsymbol{C}^i$ is the stiffness tensor of the inclusion, $\widehat{\boldsymbol{G}}$ is the elastic tensor in relation to the shape of the inclusion (when the background medium exhibits transverse isotropy, the expression of $\widehat{\boldsymbol{G}}$ can be given in the form of a line integral), $\boldsymbol{I}$ is the unit tensor.

(C) Anisotropic SCA + DEM model

To create a biconnected solid at all porosities to estimate the anisotropic properties, the expression for the effective compliances of the composite material is given by Hornby (1994) below:

$$\boldsymbol{s}^* = \boldsymbol{s}^0 - \sum_{n=1}^{N} v_n\left(\boldsymbol{s}^0\boldsymbol{c}^n - \boldsymbol{I}\right)\boldsymbol{K}^n \tag{C.1}$$

where $\boldsymbol{s}^*$ and $\boldsymbol{s}^0$ are the compliance tensors of the effective material and the rock matrix, v_n and $\boldsymbol{c}^n$ are the volume and stiffness tensors of the n-th component, $\boldsymbol{I}$ is unit tensor, $\boldsymbol{K}^n$ is the tensor that connects the average stress of the composite material with the average strain of each phase inside.

Treat each of the composites as equal, we replace the matrix material in the model with the effective material, we set $\boldsymbol{c}^0 = \boldsymbol{c}^{\mathrm{SCA}}$. Then Eq. (C.1) becomes:

$$\sum_{n=1}^{N} \boldsymbol{v}_n\left(\boldsymbol{c}^n - \boldsymbol{c}^{\mathrm{SCA}}\right)\boldsymbol{K}^{*n} = 0 \tag{C.2}$$

where $\boldsymbol{K}^{*n}$ depends on the solution, rearranging $\boldsymbol{c}^{\mathrm{SCA}}$, we get:

$$\boldsymbol{c}^{\mathrm{SCA}} = \sum_{n=1}^{N} v_n \boldsymbol{c}^n \boldsymbol{K}^{*n} \left\{ \sum_{p=1}^{N} v_p \boldsymbol{K}^{*p} \right\}^{-1} \tag{C.3}$$

To solve this equation, we need to first give the initial value of $\boldsymbol{c}^{\mathrm{SCA}}$, calculate the above equation to get a new $\boldsymbol{c}^{\mathrm{SCA}}$, iterate on the right side of the above equation again, and iterate again until $\boldsymbol{c}_n^{\mathrm{SCA}} = \boldsymbol{c}_{n-1}^{\mathrm{SCA}}$.

According to the eigenstrain problem, the expression for the tensor $\boldsymbol{K}^{*n}$ can be obtained:

$$\boldsymbol{K}^{*n} = \left[\boldsymbol{c}^{\mathrm{SCA}} \left(\boldsymbol{I} + \widehat{\boldsymbol{G}}_{ijkl} \left(\boldsymbol{c}^n - \boldsymbol{c}^{\mathrm{SCA}} \right) \right) \right]^{-1} \tag{C.4}$$

where $\widehat{\boldsymbol{G}}_{ijkl} = \frac{1}{8\pi}(\overline{\boldsymbol{G}}_{ikjl} + \overline{\boldsymbol{G}}_{jkil})$, $\overline{\boldsymbol{G}}$ is the elastic tensor in relation to the shape of the inclusion, when the background medium exhibits transverse isotropy, the expression for $\overline{\boldsymbol{G}}$ can be given in the form of a line integral.

From this, the expression of the anisotropic SCA model can be obtained:

$$\begin{aligned} \boldsymbol{c}^{\mathrm{SCA}} = & \sum_{n=1}^{N} v_n \boldsymbol{c}^n \left(\boldsymbol{I} + \widehat{\boldsymbol{G}} \left(\boldsymbol{c}^n - \boldsymbol{c}^{\mathrm{SCA}} \right) \right)^{-1} \\ & \left\{ \sum_{p=1}^{N} v_p \left(\boldsymbol{I} + \widehat{\boldsymbol{G}} \left(\boldsymbol{c}^p - \boldsymbol{c}^{\mathrm{SCA}} \right) \right)^{-1} \right\}^{-1} \end{aligned} \tag{C.5}$$

Hornby's equivalent compliance tensor expression for composites is organized into a differential form:

$$\boldsymbol{s}^*(v + \Delta v) = \boldsymbol{s}^*(v) - \frac{\Delta v}{(1 - v)} \left(\boldsymbol{s}^*(v) \boldsymbol{c}^i - \boldsymbol{I} \right) \boldsymbol{K}^i (v + \Delta v) \tag{C.6}$$

When $\Delta v \to 0$, substituting the expression of tensor $\boldsymbol{K}$ into the above equation gives the expression of the anisotropic DEM model:

$$\begin{aligned} \frac{\mathrm{d}}{\mathrm{d}V} \left(\boldsymbol{C}^{\mathrm{DEM}}(V) \right) = & \frac{1}{1 - V} \left(\boldsymbol{C}^i \right. \\ & \left. - \boldsymbol{C}^{\mathrm{DEM}}(V) \right) \left[\boldsymbol{I} + \widehat{\boldsymbol{G}} \left(\boldsymbol{C}^i - \boldsymbol{C}^{\mathrm{DEM}}(V) \right) \right]^{-1} \end{aligned} \tag{C.7}$$

Given that the anisotropic SCA model effectively ensures the interconnectivity of clay fluids within duplex rocks solely within a porosity range of 40%–60%, it becomes imperative to integrate the SCA and DEM methodologies when estimating the effective elastic parameters of such systems. To accurately mimic the genuine two-phase structure of clay and water in rocks, we initially employ the anisotropic SCA model to compute the equivalent stiffness tensor for a two-phase mixture containing 50% fluid content. Subsequently, we leverage the anisotropic DEM model to fine-tune these calculations to align with the specific porosity characteristics of the rock, thereby deriving the comprehensive results from the combined anisotropic SCA + DEM approach. This combined strategy ensures a more precise and realistic portrayal of the mechanical behavior of the two-phase mixture.

(D) C&S model

Ciz and Shapiro (2007) formulated a theory centered on the concept of solid skeleton and pore material, incorporating the fundamental assumption of infinitesimal strain. They postulated that the pores within the rock are uniformly distributed, maintaining a balanced pore pressure throughout. By ingeniously extending the Gassmann fluid substitution equation to encompass solid replacement, they derived a novel equation, which has since been widely recognized as the C&S equation.

$$\begin{aligned} K_{\mathrm{sat}}^{-1} &= K_{\mathrm{dry}}^{-1} - \frac{\left(K_{\mathrm{dry}}^{-1} - K_{\mathrm{gr}}^{-1} \right)^2}{\phi \left(K_{\mathrm{if}}^{-1} - K_{\mathrm{gr}}^{-1} \right) + \left(K_{\mathrm{dry}}^{-1} - K_{\mathrm{gr}}^{-1} \right)}, \\ \mu_{\mathrm{sat}}^{-1} &= \mu_{\mathrm{dry}}^{-1} - \frac{\left(\mu_{\mathrm{dry}}^{-1} - \mu_{\mathrm{gr}}^{-1} \right)^2}{\phi \left(\mu_{\mathrm{if}}^{-1} - \mu_{\mathrm{gr}}^{-1} \right) + \left(\mu_{\mathrm{dry}}^{-1} - \mu_{\mathrm{gr}}^{-1} \right)}, \end{aligned} \tag{D.1}$$

where, K_{sat} and μ_{sat} represent the effective bulk modulus and shear modulus of the rock, respectively, after the pore-filling material (solid or fluid) has been incorporated. K_{dry} and μ_{dry}, on the other hand, denote the bulk modulus and shear modulus of dry rock, respectively. Additionally, K_{if} and K_{gr} signify the bulk modulus of pore material and rock matrix particles, while μ_{if} and μ_{gr} represent their shear moduli, respectively. Φ represents the total porosity of the rock.

(E) Anisotropic tensile strength criterion

SPW Criterion: Jaeger (1960) first proposed the single weak plane theory to theoretically describe strength anisotropy. Lee and Pietruszczak (2015) generalized the SPW criterion for layered rocks by assuming that each physical plane except the weak plane has the same tensile strength, based on the original SPW criterion. Since the tensile strength of weak planes is typically much lower than that of intact rock materials, tensile failure is likely to occur along the weak plane when its inclination is less than a critical value:

$$T(\theta) = \begin{cases} \dfrac{T_0}{\cos^2 \theta} & 0^\circ \le \theta \le \theta^* \\ T_{90} & \theta^* \le \theta \le 90^\circ \end{cases} \tag{E.1}$$

where the critical angle θ^* is defined as: $\theta^* = \cos^{-1} \sqrt{\frac{T_0}{T_{90}}}$

L-P Criterion: Lee and Pietruszczak (2015) proposed a new two-dimensional anisotropic tensile strength criterion by combining the N-Z criterion with Cauchy's formula.

$$T(\theta) = \frac{(t_0 + T_{90})}{2} - \frac{(t_{90} + T_0)}{2} \cos 2\theta \tag{E.2}$$

This equation assumes that the directional variation of tensile strength with orientation θ is completely defined by T_{90} (the maximum value) and T_0 (the minimum value).

CPA Criterion: Lee and Pietruszczak (2015) proposed the anisotropic tensile strength CPA (Critical Plane Approach) criterion by generalizing the tensile failure criterion for orthotropic media to a spatial framework, based on the critical plane approach and using a second-order tensor to characterize the directional deviation of tensile strength spatial distribution.

$$\begin{aligned} T(\theta) = & \frac{T_0 \exp(-\Omega_0) - T_{90} \exp(2\Omega_0)}{\exp(-\Omega_0) - \exp(2\Omega_0)} \\ & + \frac{T_0 - T_{90}}{\exp(-\Omega_0) - \exp(2\Omega_0)} \exp\left[\Omega_0 \left(3\cos^2 \theta - 1 \right) \right] \end{aligned} \tag{E.3}$$

where Ω_0 is a strength spatial distribution parameter that accommodates a higher degree of anisotropy.

P-Q Criterion: Liu et al. (2022) conducted direct tensile tests on slate samples and derived a new phenomenological tensile failure criterion for anisotropic rocks, namely the P-Q criterion, by introducing an anisotropic coefficient ξbased on the N-Z criterion.

$$T(\theta) = \frac{T_0 T_{90}}{T_0 + (t_{90} - T_0)\cos^n\theta} \tag{E.4}$$

where T_0 is the minimum tensile strength, and T_{90} is the maximum tensile strength.

References

Ai, C., Zhang, J., Li, Y., et al., 2016. Estimation criteria for rock brittleness based on energy analysis during the rupturing process. Rock Mech. Rock Eng. 49, 4681–4698. https://doi.org/10.1007/s00603-016-1078-x.

Alejano, L.R., González-Fernández, M.A., Estévez-Ventosa, X., et al., 2021. Anisotropic deformability and strength of slate from NW-Spain. Int. J. Rock Mech. Min. Sci. 148, 104923. https://doi.org/10.1016/j.ijrmms.2021.104923.

Altindag, R., 2002. The evaluation of rock brittleness concept on rotary blast hole drills. J. South Afr. Inst. Min. Metall. 102 (1), 61–66. https://doi.org/10.10520/AJA0038223X_2763.

Baird, A.F., Kendall, J.M., Fisher, Q.J., Budge, J., 2017. The role of texture, cracks, and fractures in highly anisotropic shales. J. Geophys. Res. 122 (12), 10341–10351. https://doi.org/10.1002/2017JB014710.

Berryman, J.G., 1980. Long-wavelength propagation in composite elastic media. I. spherical inclusions. J. Acoust. Soc. Am. 68 (6), 1809–1819. https://doi.org/10.1121/1.385172.

Berryman, J.G., 1992. Single-scattering approximations for coefficients in Biot's equations of poroelasticity. Acoust. Soc. Am. 91, 551–571. https://doi.org/10.1121/1.402518.

Berryman, J.G., 1995. Mixture theories for rock properties. In: Ahrens, T.J. (Ed.), Rock Physics and Phase Relations: a Handbook of Physical Constants. AGU Reference Shelf 3. American Geophysical Union, Washington, DC, pp. 205–228. https://doi.org/10.1029/rf003p0001.

Bieniawski, Z.T., Hawkes, I., 1978. Suggested methods for determining tensile strength of rock materials. Int. J. Rock Mech. Min. Sci. Geomech. Abstr. 15 (3), 99–103. https://doi.org/10.1016/0148-9062(78)90003-7.

Chen, G.Q., Wu, J.C., Jiang, W.Z., 2020. An evaluation method of rock brittleness based on the whole process of elastic energy evolution. Chin. J. Rock Mech. Eng. 39 (5), 901–911. https://doi.org/10.13722/j.cnki.jrme.2019.1161 (in Chinese).

Cho, D., Perez, M., 2014. Rock quality assessment for hydraulic fracturing: a rock physics perspective. SEG Technical Program Expanded Abstracts, pp. 2814–2818. https://doi.org/10.1190/segam2014-1624.1.

Ciz, R., Shapiro, S., 2007. Generalization of Gassmann equations for porous media saturated with a solid material. Geophysics 72 (6), A75–A79. https://doi.org/10.1190/1.2772400.

Colak, K., Unlu, T., 2004. Effect of transverse anisotropy on the Hoek–Brown strength parameter 'm_i' for intact rocks. Int. J. Rock Mech. Min. Sci. 41 (6), 1045–1052. https://doi.org/10.1016/j.ijrmms.2004.04.004.

Cooper, J., Stamford, L., Azapagic, A., 2016. Shale gas: A review of the economic, environmental, and social sustainability. Energy Technol. 4 (7), 772–792. https://doi.org/10.1002/ente.201500464.

Feng, G., Kang, Y., Sun, Z., et al., 2019. Effects of supercritical CO_2 adsorption on the mechanical characteristics and failure mechanisms of shale. Energy 173, 870–882. https://doi.org/10.1016/j.energy.2019.02.069.

Feng, G, Kang, Y, Wang, X, et al., 2020. Investigation on the failure characteristics and fracture classification of shale under Brazilian test conditions. Rock Mech. Rock Eng. 53, 3325–3340. https://doi.org/10.1007/s00603-020-02110-6.

Gale, J.F.W., Reed, R.M., Holder, J., 2007. Natural fractures in the Barnett Shale and their importance for hydraulic fracture treatments. AAPG Bull. 91 (4), 603–622. https://doi.org/10.1306/11010606061.

Geng, Z., Chen, M., Jin, Y., et al., 2016. Experimental study of brittleness anisotropy of shale in triaxial compression. J. Nat. Gas Sci. Eng. 36, 510–518. https://doi.org/10.1016/j.jngse.2016.10.059.

Goodway, B, Perez, M, Varsek, J, et al., 2010. Seismic petrophysics and isotropic-anisotropic AVO methods for unconventional gas exploration. Lead. Edge 29 (12), 1500–1508. https://doi.org/10.1190/1.3525367.

Grieser, B., Bray, J., 2007. Identification of production potential in unconventional reservoirs. SPE Production and Operations. https://doi.org/10.2118/106623-MS.

Gui, J., Guo, J., Sang, Y., et al., 2023. Evaluation on the anisotropic brittleness index of shale rock using geophysical logging. Petroleum 9 (4), 545–557. https://doi.org/10.1016/j.petlm.2022.06.001.

Guo, T., 2016. Key geological issues and main controls on accumulation and enrichment of Chinese shale gas. Petrol. Explor. Dev. 43 (3), 349–359. https://doi.org/10.1016/S1876-3804(16)30042-8.

Guo, J.C., Zhao, Z.H., He, S.G., et al., 2015. A new method for shale brittleness evaluation. Environ. Earth Sci. 73 (10), 5855–5865. https://doi.org/10.1007/s12665-015-4268-z.

Hajiabdolmajid, V., Kaiser, P., 2003. Brittleness of rock and stability assessment in hard rock tunneling. Tunn. Undergr. Space Technol. 18 (1), 35–48. https://doi.org/10.1016/S0886-7798(02)00100-1.

Hornby, B.E, Schwartz, L.M., Hudson, J.A., 1994. Anisotropic effective-medium modeling of the elastic properties of shales. Geophysics 59 (59), 1570–1583. https://doi.org/10.1190/1.1443546.

Hou, Z.K., Yang, C.H., Wei, X., et al., 2016. Experimental study on the brittle characteristics of Longmaxi formation shale. J. China Coal Soc. 41 (5), 1188–1196. https://doi.org/10.13225/j.cnki.jccs.2015.0957 (in Chinese).

Hucka, V., Das, B., 1974. Brittleness determination of rocks by different methods. Int. J. Rock Mech. Min. Sci. Geomech. Abstr. 11 (10), 389–392. https://doi.org/10.1016/0148-9062(74)91109-7.

Jaeger, J.C., 1960. Shear failure of anistropic rocks. Geol. Mag. 97 (1), 65–72. https://doi.org/10.1017/S0016756800061100.

Jamshidi, A., Torabi-Kaveh, M., Nikudel, M.R., 2021. Effect of anisotropy on the strength and brittleness indices of laminated sandstone. Iran. J. Sci. Technol. Trans. A Sci. 45, 927–936. https://doi.org/10.1007/s40995-021-01080-w.

Jarvie, D.M., Hill, R.J., Ruble, T.E., et al., 2007. Unconventional shale-gas systems: the Mississippian Barnett Shale of north-central Texas as one model for thermogenic shale-gas assessment. AAPG Bull. 91 (4), 475–499. https://doi.org/10.1306/12190606068.

Kartashov, É.M., 1978. Griffith energy criterion of fracture for an edge crack. Sov. Phys. J. 21 (12), 1567–1571. https://doi.org/10.1007/BF00892473.

Khaledi, K., Winhausen, L., Jalali, M., et al., 2023. Constitutive modeling of clay shales in undrained conditions and its experimental verification for Opalinus Clay. Int. J. Rock Mech. Min. Sci. 171, 105588. https://doi.org/10.1016/j.ijrmms.2023.105588.

Kivi, I.R., Ameri, M., Molladavoodi, H., 2018. Shale brittleness evaluation based on energy balance analysis of stress-strain curves. J. Pet. Sci. Eng. 167, 1–19. https://doi.org/10.1016/j.petrol.2018.03.061.

Kuang, Z.H., Qiu, S.L., Li, S.J., et al., 2021. A new rock brittleness index based on the characteristics of complete stress-strain behaviours. Rock Mech. Rock Eng. 54, 1109–1128. https://doi.org/10.1007/s00603-020-02311-z.

Lee, Y.K., Pietruszczak, S., 2015. Tensile failure criterion for transversely isotropic rocks. Int. J. Rock Mech. Min. Sci. 79, 205–215. https://doi.org/10.1016/j.ijrmms.2015.08.019.

Li, C., Xie, H., Wang, J., 2020. Anisotropic characteristics of crack initiation and crack damage thresholds for shale. Int. J. Rock Mech. Min. Sci. 126, 104178. https://doi.org/10.1016/j.ijrmms.2019.104178.

Liu, H., Zheng, J., Zhao, W., et al., 2019. A new method for evaluating brittleness index of deep tight sandstone reservoir. J. Geomech. 25 (4), 492–500. https://doi.org/10.12090/j.issn.1006-6616.2019.25.04.047 (in Chinese).

Liu, P., Liu, Q., Huang, X., et al., 2022. Direct tensile test and FDEM numerical study on anisotropic tensile strength of Kangding Slate. Rock Mech. Rock Eng. 55 (12), 7765–7789. https://doi.org/10.1007/s00603-022-03036-x.

Luan, X., Di, B., Wei, J., et al., 2014. Laboratory measurements of brittleness anisotropy in synthetic shale with different cementation. SEG Technical Program Expanded Abstracts 2014, pp. 3005–3009. https://doi.org/10.1190/segam2014-0432.1.

Mandal, P.P., Sarout, J., Rezaee, R., 2022. Triaxial deformation of the goldwyer gas shale at in situ stress conditions—Part I: anisotropy of elastic and mechanical properties. Rock Mech. Rock Eng. 55 (10), 6121–6149. https://doi.org/10.1007/s00603-022-02936-2.

Mavko, G., Mukerji, T., Dvorkin, J., 2009. The Rock Physics Handbook: Tools for Seismic Analysis of Porous Media, second ed. Cambridge University Press, Cambridge. https://doi.org/10.1017/CBO9780511626753.

Nasseri, M.H.B., Rao, K.S., Ramamurthy, T., 2003. Anisotropic strength and deformational behavior of Himalayan schists. Int. J. Rock Mech. Min. Sci. 40 (1), 3–23. https://doi.org/10.1016/S1365-1609(02)00103-X.

Niandou, H., Shao, J.F., Henry, J.P., et al., 1997. Laboratory investigation of the mechanical behaviour of Tournemire shale. Int. J. Rock Mech. Min. Sci. 34 (1), 3–16. https://doi.org/10.1016/S1365-1609(97)80029-9.

Nova, R., Zaninetti, A., 1990. An investigation into the tensile behaviour of a schistose rock. Int. J. Rock Mech. Min. Sci. Geomech. Abstr. 27 (4), 231–242. https://doi.org/10.1016/0148-9062(90)90526-8.

Nygård, R., Gutierrez, M., Bratli, R.K., Høeg, K., 2006. Brittle–ductile transition, shear failure and leakage in shales and mudrocks. Mar. Petrol. Geol. 23 (2), 201–212. https://doi.org/10.1016/j.marpetgeo.2005.10.001.

Ong, O.N., Schmitt, D.R., Kofman, R.S., et al., 2016. Static and dynamic pressure sensitivity anisotropy of a calcareous shale. Geophys. Prospect. 64 (4), 875–897. https://doi.org/10.1111/1365-2478.12403.

Parney, R., Lange, N., 2010. Comparison of seismic brittleness and anisotropy to micro-seismic in the Waltman Shale. SEG Technical Program Expanded Abstracts 2010, pp. 278–282. https://doi.org/10.1190/1.3513423.

Qian, K.R., Liu, T., Liu, J.Z., et al., 2020. Construction of a novel brittleness index equation and analysis of anisotropic brittleness characteristics for unconventional shale formations. Pet. Sci. 17 (1), 70–85. https://doi.org/10.1007/s12182-019-00372-6.

Rickman, R., Mullen, M., Petre, E., et al., 2008. A practical use of shale petrophysics for stimulation design optimization: All shale plays are not clones of the

Barnett shale. SPE Annual Technical Conference and Exhibition, SPE-115258-MS. https://doi.org/10.2118/115258-MS.
Rybacki, E., Meier, T., Dresen, G., 2016. What controls the mechanical properties of shale rocks? – Part II: brittleness. J. Pet. Sci. Eng. 144, 39–58. https://doi.org/10.1016/j.petrol.2016.02.022.
Salah, M., Mohamed, I.M., Ibrahim, M., et al., 2019. A newly developed approach to evaluate rock brittleness and fracability for hydraulic fracturing optimization in shale gas. SPE Western Regional Meeting. Society of Petroleum Engineers, SPE-195280-MS. https://doi.org/10.2118/195280-MS.
Thomsen, L., 1986. Weak elastic anisotropy. Geophysics 51 (10), 1954–1966. https://doi.org/10.1190/1.1442051.
Tsvankin, I., Gaiser, J., Grechka, V., et al., 2010. Seismic anisotropy in exploration and reservoir characterization: An overview. Geophysics 75 (5), 75A15–75A29. https://doi.org/10.1190/1.3481775.
Vernik, L., Nur, A., 1992. Ultrasonic velocity and anisotropy of hydrocarbon source rocks. Geophysics 57 (5), 727–735. https://doi.org/10.1190/1.1443286.
Wan, C., Song, Y., Li, Z., et al., 2022. Variation in the brittle-ductile transition of Longmaxi shale in the Sichuan Basin, China: the significance for shale gas exploration. J. Pet. Sci. Eng. 209, 109858. https://doi.org/10.1016/j.petrol.2021.109858.
Wang, Z., 2002. Seismic anisotropy in sedimentary rocks, part 2: laboratory data. Geophysics 67 (5), 1423–1440. https://doi.org/10.1190/1.1512743.
Wang, F.P., Gale, J.F., 2009. Screening criteria for shale-gas systems. Gulf Coast Assoc. Geol. Soc. Trans. 59, 779–793.
Wang, Q., Wang, Y., Guo, S.G., et al., 2015. The effect of shale properties on the anisotropic brittleness criterion index from laboratory study. J. Geophys. Eng. 12 (5), 866–874. https://doi.org/10.1088/1742-2132/12/5/866.
Wang, H., Liu, D., Hu, Z., et al., 2017. Mechanical properties and brittleness evaluation of layered shale rock. J. Eng. Geol. 25 (6), 1414–1423. https://doi.org/10.13544/j.cnki.jeg.2017.06.003 (in Chinese).
Wittke, W., 1990. Rock Mechanics, Theory and Applications with Case Histories. Springer-Verlag, Berlin, Heidelberg. https://doi.org/10.1007/978-3-642-88109-1.
Wu, Y., Li, Y., Luo, S., et al., 2020. Multiscale elastic anisotropy of a shale characterized by cross-scale big data nanoindentation. Int. J. Rock Mech. Min. Sci. 134, 104458. https://doi.org/10.1016/j.ijrmms.2020.104458.
Xie, J., Di, B., Wei, J., et al., 2015. Feasibility of theoretical formulas on the anisotropy of shale based on laboratory measurement and error analysis. J. Geophys. Eng. 12 (2), 253–261. https://doi.org/10.1088/1742-2132/12/2/253.
Xie, J., Zhang, J., Fang, Y., et al., 2023. Quantitative evaluation of shale brittleness based on brittle-sensitive index and energy evolution-based fuzzy analytic hierarchy process. Rock Mech. Rock Eng. 56, 3003–3021. https://doi.org/10.1007/s00603-022-03213-y.
Yagiz, S., 2009. Assessment of brittleness using rock strength and density with punch penetration test. Tunn. Undergr. Space Technol. 24 (1), 66–74. https://doi.org/10.1016/j.tust.2008.04.002.
Yan, D., Zhao, L., Wang, Y., et al., 2023. Heterogeneity indexes of unconventional reservoir shales: quantitatively characterizing mechanical properties and failure behaviors. Int. J. Rock Mech. Min. Sci. 171, 105577. https://doi.org/10.1016/j.ijrmms.2023.105577.
Yang, S.Q., Yin, P.F., Ranjith, P.G., 2020. Experimental study on mechanical behavior and brittleness characteristics of Longmaxi formation shale in Changning, Sichuan Basin, China. Rock Mech. Rock Eng. 53, 2461–2483. https://doi.org/10.1007/s00603-020-02057-8.
Yin, H., 1993. Acoustic Velocity and Attenuation of Rocks: Isotropy, Intrinsic Anisotropy, and stress-induced Anisotropy. Stanford University, Stanford. Ph.D. Thesis.
Yuan, J.L., Deng, J.G., Tan, Q., et al., 2013. Borehole stability analysis of horizontal drilling in shale gas reservoirs. Rock Mech. Rock Eng. 46, 1157–1164. https://doi.org/10.1007/s00603-012-0341-z.
Zhang, D., Ranjith, P.G., Perera, M.S.A., 2016. The brittleness indices used in rock mechanics and their application in shale hydraulic fracturing: a review. J. Pet. Sci. Eng. 143, 158–170. https://doi.org/10.1016/j.petrol.2016.08.017.
Zhao, L., Qin, X., Han, D.H., et al., 2016. Rock-physics modeling for the elastic properties of organic shale at different maturity stages. Geophysics 81 (5), D527–D541. https://doi.org/10.1190/geo2015-0713.1.
Zhao, P., Fan, X., Wang, X., et al., 2024. Geomechanical properties of laminated shale and bedding shale after water absorption: a case study of the Chang 7 shale in Ordos Basin, China. Int. J. Rock Mech. Min. Sci. 180, 105798. https://doi.org/10.1016/j.ijrmms.2024.105798.